HAL
open science

Formulation of an ocean model for global climate simulations

S. M. Griffies, A. Gnanadesikan, K. W. Dixon, J. P. Dunne, R. Gerdes, M. J. Harrison, A. Rosati, J. L. Russell, B. L. Samuels, M. J. Spelman, et al.

To cite this version:

S. M. Griffies, A. Gnanadesikan, K. W. Dixon, J. P. Dunne, R. Gerdes, et al.. Formulation of an ocean model for global climate simulations. Ocean Science Discussions, 2005, 2 (3), pp.165-246. hal-00298422

HAL Id: hal-00298422

https://hal.science/hal-00298422v1

Submitted on 18 Jun 2008

HAL is a multi-disciplinary open access archive for the deposit and dissemination of scientific research documents, whether they are published or not. The documents may come from teaching and research institutions in France or abroad, or from public or private research centers.

L'archive ouverte pluridisciplinaire **HAL**, est destinée au dépôt et à la diffusion de documents scientifiques de niveau recherche, publiés ou non, émanant des établissements d'enseignement et de recherche français ou étrangers, des laboratoires publics ou privés.

Ocean Science Discussions, 2, 165–246, 2005
www.ocean-science.net/osd/2/165/
SRef-ID: 1812-0822/osd/2005-2-165
European Geosciences Union

Ocean Science Discussions

Papers published in *Ocean Science Discussions* are under open-access review for the journal *Ocean Science*

Formulation of an ocean model for global climate simulations

S. M. Griffies[1], A. Gnanadesikan[1], K. W. Dixon[1], J. P. Dunne[1], R. Gerdes[2], M. J. Harrison[1], A. Rosati[1], J. L. Russell[3], B. L. Samuels[1], M. J. Spelman[1], M. Winton[1], and R. Zhang[3]

[1]NOAA Geophysical Fluid Dynamics Laboratory, Princeton, USA
[2]Alfred-Wegener-Institut für Polar- und Meeresforschung, Bremerhaven, Germany
[3]Program in Atmospheric and Oceanic Sciences, Princeton, USA

Received: 4 April 2005 – Accepted: 8 May 2005 – Published: 20 May 2005

Correspondence to: S. M. Griffies (stephen.griffies@noaa.gov)

© 2005 Author(s). This work is licensed under a Creative Commons License.

Abstract

This paper summarizes the formulation of the ocean component to the Geophysical Fluid Dynamics Laboratory's (GFDL) coupled climate model used for the 4th IPCC Assessment (AR4) of global climate change. In particular, it reviews elements of ocean climate models and how they are pieced together for use in a state-of-the-art coupled model. Novel issues are also highlighted, with particular attention given to sensitivity of the coupled simulation to physical parameterizations and numerical methods. Features of the model described here include the following: (1) tripolar grid to resolve the Arctic Ocean without polar filtering, (2) partial bottom step representation of topography to better represent topographically influenced advective and wave processes, (3) more accurate equation of state, (4) three-dimensional flux limited tracer advection to reduce overshoots and undershoots, (5) incorporation of regional climatological variability in shortwave penetration, (6) neutral physics parameterization for representation of the pathways of tracer transport, (7) staggered time stepping for tracer conservation and numerical efficiency, (8) anisotropic horizontal viscosities for representation of equatorial currents, (9) parameterization of exchange with marginal seas, (10) incorporation of a free surface that accomodates a dynamic ice model and wave propagation, (11) transport of water across the ocean free surface to eliminate unphysical "virtual tracer flux" methods, (12) parameterization of tidal mixing on continental shelves.

1. Introduction

The purpose of this paper is to detail the formulation of the ocean model developed by scientists and engineers at NOAA's Geophysical Fluid Dynamics Laboratory (GFDL) for use in our latest coupled global climate model. This paper is one in a series from GFDL, including Delworth et al. (2005), Gnanadesikan et al. (2005), Wittenberg et al. (2005), and Stouffer et al. (2005). The focus in the present paper is on the numerical algorithms and physical parameterizations which form the fundamentals of the ocean

model component. Some of this paper takes the form of a review. We hope that this format is useful for readers aiming to understand what is involved with constructing global models. We also highlight some novel scientific issues related to sensitivity of the coupled simulation to (1) the use of real water fluxes rather than virtual tracer fluxes, including the treatment of river runoff and exchange with semi-enclosed basins, (2) the algorithm for time stepping the model equations, (3) sensitivity of the extra-tropical circulation to horizontal viscosity, and (4) treatment of the neutral physical parameterizations.

1.1. Documentation of ocean climate models

Many issues forming the fundamental elements of ocean climate models are often briefly mentioned in papers primarily concerned with describing simulation characteristics, or they may be relegated to non-peer reviewed technical reports. Such discussions often leave the reader with little intellectual or practical appreciation for the difficult and critical choices made during model development. Our goal here is to partially remedy this situation by focusing on numerical and physical details of the most recent GFDL ocean climate model. In so doing, we expose some of the guts of the model and attempt to rationalize choices. Along the way, we identify places where further research and development may be warranted.

This paper is written on the premise that the evolution of ocean climate science is facilitated by a candid peer-reviewed discussion of the interdependent and nontrivial choices that developers make in constructing global climate models. The importance of such discussions has grown during the past decade as the models are used for an increasing variety of applications, many of which, such as climate change projections, garner intense scrutiny from non-scientific communities. Additionally, full disclosure is necessary for modelers to reproduce results of each other, and thus to enhance the scientific robustness of climate modelling.

We admittedly fall short of fully realizing our goals in writing this paper. First, choices were made to balance conciseness with completeness. A substantially longer paper

with more thorough analysis of sensitivity experiments is required to satisfy the completeness goal. Some of these experiments will form the basis of separate studies. Second, we are limited by focusing on one particular climate model, that from GFDL contributing to AR4. Comparisons with other models go beyond the scope of this study, but such would certainly assist in understanding causes for the many differences found in climate model simulations.

Given the above limitations, we remain hopeful that this paper serves as a step towards full disclosure of the rationale forming the basis for a particular ocean climate model. We believe such provides the climate science community with a useful resource for understanding both how to reproduce elements of what we have done, and to expose areas where further research and development is warranted.

1.2. Comments on ocean climate model development

One of the first global coupled climate models was that of Manabe and Bryan (1969). Their model used an early version of the GFDL geopotential vertical coordinate ocean model based on the work of Bryan and Cox (1967) and Bryan (1969b), with Bryan (1969a) documenting algorithms used in this model. It is notable that such z-models, which typically employ the hydrostatic and Boussinesq approximations, still comprise the vast majority of ocean models used for climate simulations (see Griffies et al., 2000a, for a review). In particular, all versions of the GFDL coupled climate models to date have employed this class of ocean model.

In most z-models used for climate studies through the early 1990's, the ocean primitive equations were discretized using spherical coordinates for the lateral directions, with vertical positions at fixed depths for all latitude and longitude points, and with grid cells of time independent volumes. Additionally, physical processes such as ocean tracer transport were aligned according to this grid. Since the middle 1990's, there have been fundamental advances to this older model formulation that significantly enhance the physical integrity of z-model simulations (see Griffies et al., 2000a, for a review). It is therefore important to include these advances in the ocean climate mod-

els used for realistic climate simulations.

There are two main ways in which climate modellers seek realism in their simulations. First, the resultant simulation should behave like the observed climate. Second, individual physical processes should be represented or parameterized to the best of our understanding. As documented in Delworth et al. (2005), Wittenberg et al. (2005), Stouffer et al. (2005), and Gnanadesikan et al. (2005), the CM2 model series produces a climate that is relatively realistic in terms of its overall simulation. This document presents how we have addressed criticisms of previous GFDL models with regard to unrealistic representations of physical processes. We also highlight algorithm features that can result in significant changes in the model efficiency, stability, and simulation characteristics.

1.3. Models discussed in this paper

Throughout this paper, we focus on two versions of the latest GFDL coupled climate model: CM2.0 and CM2.1. These versions have corresponding ocean model versions denoted OM3.0 and OM3.1. The model versions differ in the following ways.

The first difference is in the atmospheric component. CM2.0 uses a B-grid dynamical core documented by Anderson et al. (2005). CM2.1 uses the finite volume core of Lin (2004). Both atmospheric models use similar physical parameterizations. As discussed in Delworth et al. (2005), the mid-latitude storm tracks in both hemispheres are shifted poleward in CM2.1 relative to CM2.0, with the largest shift (order 3–4°) in the Southern Hemisphere. This wind shift causes a nontrivial change in the ocean circulation in both hemispheres that significantly reduces middle to high latitude ocean biases in CM2.1 relative to CM2.0 (see Delworth et al., 2005; Gnanadesikan et al., 2005, for full discussion).

The second difference is in the ocean model, with motivation for these changes provided in this paper. These differences are the following.

- OM3.0 uses a leap frog for the time tendency, whereas OM3.1 uses a staggered

two time step tendency.

- OM3.1 uses a constant neutral diffusivity of $600 m^2 s^{-1}$. OM3.0 uses a nonconstant diffusivity equal to the skew diffusivity, and this diffusivity is generally less than the $600 m^2 s^{-1}$ used in OM3.1.

- OM3.0 uses five times larger background horizontal viscosity poleward of 20° than OM3.1.

1.4. Organization of this paper

This paper consists of two main sections along with an appendix. In Section 2, we summarize how various methods and parameterizations documented in other studies have been incorporated into our ocean climate model. This section represents a review of certain elements of ocean climate modelling that have been found to be critical in the construction of our model. Section 3 focuses on experiences and methods that are novel to this work. In particular, Sect. 3.1 explores the issues involved with switching from the commonly used virtual tracer fluxes to real water forcing. We then discuss time stepping algorithms in Sect. 3.2, where we highlight the fundamental benefits of a newly implemented "time staggered" scheme. Neutral physics parameterizations are described in Sect. 3.3, where we note the reasons for changing the subgrid scale (SGS) parameters mentioned above. Horizontal friction is presented in Sect. 3.4, where we show the rather large sensitivity of the simulation to the reduction in extra-tropical viscosity. Section 3.5 details our method for exchanging water mass properties between the open ocean and semi-enclosed basins, and Sect. 3.6 presents our approach for inserting river runoff into the ocean model. Both topics require some novel considerations due to our use of real water fluxes rather than virtual tracer fluxes. We close the paper in Sect. 4 with general comments about ocean climate model development. An appendix of model equations is given to support many discussions in the main text.

2. Elements of the ocean model based on other work

When constructing an ocean climate model, it is necessary to choose from amongst a multitude of possible numerical and physical methods. We present here a compendium of model features that have been documented in other studies which are essential elements to our ocean climate model. The main aim here is to motivate choices.

Our discussion of choices made in this section is arguably brief. We are at fault, for example, for not providing illustrations of the sensitivity of our model to alternative choices. For example, when describing the model's tripolar gridding of the sphere in Sect. 2.1, we argue for its benefits over the more traditional spherical grid. Yet we do not provide a direct comparison of simulations with and without the tripolar grid. Instead, this choice, and many others, are based on the judgement and experience of the developers. Thorough model sensitivity experiments and analysis are not available to justify every model choice. Human, computer, and time limitations preclude such. Nonetheless, these choices are acknowledged, as they are important for defining the model fundamentals as well as its simulation.

2.1. Tripolar grid

It has become common in the past decade for global ocean models to remove the Arctic Ocean's spherical coordinate singularity via a coordinate transformation to a non-spherical set of generalized orthogonal coordinates. In these models, the coordinate singularity is hidden over land. Removing the coordinate singularity allows modelers to jettison polar filtering commonly used in spherical coordinate global models (Bryan et al., 1975; Pacanowski and Griffies, 1999)[1]. Although for some purposes

[1]Polar filtering in a z-model is far less straightforward than in terrain following models typically used for atmospheric simulations. For z-models, land-sea boundaries split the filtered latitudes into distinct sectors which preclude an efficient decomposition of model fields into Fourier modes. As a result, ocean simulations become quite noisy in polar filtering regions, even though the goal of filtering is to smooth the fields by removing small scales. Filtering in

inconvenient for the Arctic (e.g. meridional transports), the spherical grid is very useful elsewhere in the World Ocean. For example, grid refinement for better representation of the equatorial wave guide is straightforward in a spherical grid. Furthermore, aligning the grid with constant latitude and longitude circles outside the Arctic simplifies the analysis of zonal and meridional transports of properties such as mass and heat.

For the above reasons, in the design of OM3 a primary aim was to remove the spherical coordinate singularity in the Arctic Ocean without affecting the region south of the Arctic. The tripolar grid of Murray (1996) (see his Fig. 7) has proven to be an effective means to achieve this goal, as well as to more evenly distribute grid points within the Arctic region than available with a spherical grid. This tripolar grid is a composite of two grids, with a familiar spherical, or latitude-longitude, grid south of 65° N. In the Arctic north of 65° N, the grid switches to a bipolar region with coordinate singularities over Siberia and Canada. The grid switch introduces a discontinuity in the derivative of the meridional grid spacing at 65° N. We have found no sign of this discontinuity in the fields (e.g. tracers, velocity, surface height) simulated on this grid. A similar grid, with smoother transition to a bipolar Arctic, has been implemented by Madec and Imbard (1996). In general, the tripolar grids have three coordinate singularities (two in the Arctic and one in the Antarctic), all of which are hidden inside land masses and so they play a negligible role in setting the model time step. Both the ocean and sea ice models in CM2 use the same grid.

Figure 1 presents the land-sea mask within the bipolar Arctic region, along with a few grid lines. The grid is logically rectangular, which makes the transition from the spherical region to the bipolar region transparent in the model algorithms. Additionally, as revealed by Fig. 7 of Murray (1996), the coordinate lines transition into the Arctic in a way that facilitates sensible diagnostics, such as transport streamfunctions and poleward heat transport, when summing along constant i-lines. This property greatly simplifies the analysis of model output. In general, the tripolar grid has proven to be a very effective gridding of the global ocean, and we have successfully used it in

general adds an unphysical, and often nontrivial, extra term to the prognostic equations.

various GFDL ocean models, both in MOM4.0 and the Hallberg Isopycnal Model (HIM) (Hallberg, 1997).

2.2. Horizontal grid resolution

Many features of the ocean circulation occur on very small spatial scales. Boundary currents such as the Gulf Stream and Kuroshio are less than 100km in width, and the dynamics that determine their separation points likely involve even smaller spatial scales. Many key passages between ocean basins such as the Bering Strait, Indonesian Throughflow, and Faeroe Bank Channel involve channels that are very narrow. This is a special problem in B-grid models like MOM, which require passages to be two tracer points in width in order for flow to occur. For this reason alone, there is considerable motivation to refine ocean model resolution. However computational limitations preclude an indefinite refinement. Consequently, resolution in climate models is refined as best as possible, while still allowing for a reasonable model computational throughput. In order to perform multiple multicentury runs to investigate anthropogenic climate change, models must be able to run at speeds of 2–5 years/day on a given computational platform. At a nominal resolution of 1°, our current generation of models run at the upper end of this range when run in physical mode only, but at the lower end when run with models of ocean biogeochemistry.

Enhancements to the meridional resolution were made in the tropics, where meridionally narrow features such as the equatorial undercurrent play an important role in tropical dynamics and variability. Previous work in forecasting such phenomena (Latif et al., 1998; Schneider et al., 2003) has indicated that meridional resolution on the order of 1/3° is required. The meridional resolution gradually transitions from 1° at 30° to 1/3° at the equator. Figure 2 illustrates the grid spacing in the model.

2.3. Vertical grid resolution

The vertical grid spacing in OM3 was chosen with attention given to the model's ability to represent the equatorial thermocline as well as processes occuring in the subtropical planetary boundary layer. For this purpose, we placed 22 evenly spaced cells in the upper 220 m, and added 28 more cells for the deeper ocean with a bottom at 5500 m (see Fig. 3).

The representation of solar shortwave penetration into the upper ocean in the presence of chlorophyll (see Sect. 2.7) may warrant even finer vertical resolution than that used here (Murtugudde et al., 2002). Other air-sea interaction processes may likewise call for increasingly refined upper ocean resolution. Unfortunately, the use of top grid cells thinner than roughly 10 m can lead to the cells vanishing when run with realistic forcing, especially with pressure loading from sea ice (see discussion in Griffies et al., 2001). Indeed, even with 10 m upper cells, we have found it necessary to limit the overall pressure from sea ice felt by the ocean surface to no more than that applied by 4 m thick ice. Ice thickness greater than 4m is assumed to exert no pressure on the sea surface.

This situation signals a fundamental limitation of free surface methods in z-models. In these models, only the upper grid cell feels motion of the surface height. Refined vertical cells in the presence of a realistically undulating ocean surface height requires alternative vertical coordinates (Griffies et al., 2000a). This issue is a topic of current research and development[2].

2.4. Bottom topography and bottom flows

It is common in z-models to have model grid cells at a given discrete level have the same thickness. In these models, it is difficult to resolve weak topographic slopes with-

[2]For example, the proposal by Adcroft and Campin (2004) to use the vertical coordinate of Stacey et al. (1995) for global modelling is of interest given its ability to resolve this problem while maintaining other features familiar to the z-models.

out including uncommonly fine vertical and horizontal resolution. This limitation can have important impacts on the model's ability to represent topographically influenced advective and wave processes. The "partial step" methods of Adcroft et al. (1997) and Pacanowski and Gnanadesikan (1998) have greatly remedied this problem via the implementation of more realistic representations of the solid earth lower boundary. Here, the vertical thickness of a grid cell at a particular discrete level does not need to be the same. This added freedom allows for a smoother, and more realistic, representation of topography by adjusting the bottom grid cell thickness to more faithfully contour the topography. Fig. 4 illustrates the bottom realized with the OM3 grid along the equator. Also shown is a representation using an older "full step" model with the same horizontal and vertical resolution. The most visible differences between full step and partial step topography are in regions where the topographic slope is not large, whereas the differences are minor in steeply sloping regions.

The topography used in OM3 was initially derived from a dataset assembled at the Southampton Oceanography Centre for use in their global eddying simulations (Andrew Coward, personal communication). This dataset is a blend of several products. Between 72° S and 72° N, version 6.2 of the satellite-derived product of Smith and Sandwell (1997) was mapped from the original Mercator projection onto a latitude-longitude grid at a resolution of 2 min. North of 72° N, a version of the International Bathymetric Chart of the Oceans (Jakobssen et al., 2000) was used, while south of 72° S the ETOPO5 product was used (NOAA, 1988).

As mentioned in Sect. 2.2, MOM4.0 is a B-grid model in which tracer points are staggered relative to velocity points. This grid arrangement necessitates the use of no-slip sidewall conditions for realistic geometries[3]. Opening channels for advective flow between basins requires the channels to be at least two tracer gridpoints wide. In the presence of complex topography not aligned with the grid, ensuring that basins which are connected in Nature are also connected within the model requires us to dig out

[3]Topography tuning must also be combined with viscosity tuning (Sect. 3.4) due to the no-slip condition which strongly affects circulation through narrow passages.

some passages. Significant attention was paid to the North Atlantic overflows (Denmark Strait, Iceland-Scotland Overflow, Faeroe Bank Channel) based on the work of Roberts and Wood (1997) suggesting that representation of the sill topography makes important differences in the circulation within the Hadley Centre's coupled model. Significant attention was also paid to the topography in the Caribbean Sea as well as the Indonesian Archipelago, where previous work suggests that the exact location of important islands can determine the throughflow in key passages like the Florida, Timor, and Lombok Straits (Wajsowicz, 1999). The resulting bottom depth field used in OM3 is shown in Fig. 5.

In general, the OM3 bottom topography was arrived at via an extended multi-step process starting originally from the Southampton dataset. Unfortunately, the numerous individual steps were not completely documented, in part because of the use of early versions of the grid generation code that contained errors, and in part because of the hundreds of subjective changes. Additionally, much development work for OM3, including its topography, used a coarser resolution model (the OM2 model). The initial version of the OM3 topography was generated by interpolating the OM2 bathymetry to the finer OM3 grid, and was followed by the subjective modification of hundreds of individual grid depths in an effort to better represent the coastlines and the major bathymetric features (e.g. sills, ridges, straits, basin interconnections) of the World Ocean.

Partial steps do not enhance the z-model's ability to represent, or to parameterize, dense flows near the bottom which often occur in regions where the topographic slope is nontrivial. Indeed, as described by Winton et al. (1998), z-models used for climate rarely resolve the bottom boundary layer present in much of the World Ocean. As a result, dense water flowing from shallow marginal seas into the deeper ocean (e.g. Denmark Strait and Strait of Gibraltar), tend to entrain far more ambient fluid than observed in Nature. This spurious entrainment dilutes the dense signals as they enter the larger ocean basins, thus compromising the integrity of simulated deep water masses.

As reviewed by Beckmann (1998) and Griffies et al. (2000a), there have been various

methods proposed to remedy problems simulating overflows in z-models. In OM3, we implemented the sigma diffusive element of the scheme proposed by Beckmann and Döscher (1997) and Döscher and Beckmann (1999). This scheme enhances downslope diffusion within the bottom cells when dense water lies above light water along a topographic slope. Unfortunately, as implemented within the partial step framework, it is possible that the partial steps could become far smaller (minimum 10 m used here) than a typical bottom boundary layer (order 50 m–100 m). In such cases, the diffusive scheme is unable to move a significant amount of dense water downslope through regions with thin partial steps. A more promising method is to increase the bottom partial step thickness in regions where overflows are known to be important, or to allow for the sigma diffusion to act within more than just the bottom-most grid cell. We did not pursue either approach for OM3 due to limitations in development time. As a result, the sigma diffusion scheme has a negligible impact on the OM3's large-scale circulation, as evidenced by its very small contribution to the meridional transport of heat (not shown).

Although partial steps may be a cause for the insensitivity of the simulation to the sigma diffusion scheme, our results are consistent with those reported by Doney and Hecht (2002), who used the same scheme but in a full step bottom topography model. We are uncertain whether the small impact of the overflow scheme in the coupled model is related to limitations of the overflow scheme algorithm, or to problems with the surface boundary forcing. Hence, although discouraging, we believe these results warrant further focused investigation in process studies and global climate models, especially given the encouraging results from idealized simulations discussed by Beckmann and Döscher (1997) and Döscher and Beckmann (1999).

2.5. Equation of state

Ocean density is fundamental to the computation of both the pressure and physical parameterizations. Hence, an accurate density calculation is required over a wide range of potential temperature, salinity, and pressure. There are two methods we use

to help make the calculation more accurate in CM2.

Density at a model time step τ is a function of pressure, potential temperature, and salinity at the same time step. However, in a hydrostatic model, pressure is diagnosed only once density is known. Some climate models (e.g. Bryan and Cox, 1972) resolve this causality loop by approximating the pressure as $p = -\rho_o\, g\, z$, which is the hydrostatic pressure at a depth $z<0$ for a fluid of uniform density ρ_o. A more accurate method was suggested by Griffies et al. (2001), whereby

$$\rho(\tau) = \rho[\theta(\tau), s(\tau), p(\tau - \Delta\tau)], \tag{1}$$

with pressure used in the equation of state lagged by a single model time step relative to potential temperature and salinity. As recommended by Dewar et al. (1998), we include contributions from the undulating surface height and loading from the sea ice for the pressure used in the density calculation.

Previous versions of MOM used the cubic polynomial approximation of Bryan and Cox (1972) to fit the UNESCO equation of state documented in Gill (1982). This approach has limitations that are no longer acceptable for global climate modelling. For example, the polynomials are fit at discrete depth levels. The use of partial step topography makes this approach cumbersome since with partial steps, it is necessary to compute density at arbitrary depths. Additionally, the cubic approximation is inaccurate for many regimes of ocean climate modelling, such as wide ranges in salinity associated with rivers and sea ice. For these two reasons, a more accurate equation of state is desired.

Feistel and Hagen (1995) updated the UNESCO equation of state by using more recent empirical data. In MOM4.0 we utilize a 25 term fit to their work developed by McDougall et al. (2003). The fit is valid for a very wide range of salinity, potential temperature, and pressure that is more than adequate for ocean climate purposes[4].

[4]The McDougall et al. (2003) equation of state is fit over a pressure range from 0 db to 8000 db. The salinity range is 0–40 psu for pressures less than 5500 db, and 30–40 psu for pressures greater than 5500 db. The potential temperature range is freezing to 33°C for pres-

2.6. Tracer advection

As physical climate models evolve to include chemical and biological models appropriate for the full earth system, they incorporate an increasingly wide array of tracers whose transport is greatly affected by strong spatial gradients in the presence of refined flow features. Many of the earlier compromises with tracer transport are unacceptable with these new model classes. In particular, previous versions of the GFDL ocean climate model used the second order centered tracer advection scheme. Upon recognizing that this scheme is too dispersive, later model versions incorporated the "Quicker" scheme. Quicker is a third order upwind biased scheme based on the work of Leonard (1979), with Holland et al. (1998) and Pacanowski and Griffies (1999) discussing implementations in ocean climate models. The Quicker scheme is far less dispersive than the second order centered scheme, thus reducing the level of spurious extrema realized in the simulation. However, as with centered differences, problems can occur with unphysical tracer extrema, in particular in regions where rivers enter the ocean thus creating strong salinity gradients. Additional problems can arise with a prognostic biogeochemistry model, where even slightly negative biological concentrations can lead to strongly unstable biological feedbacks.

There are many advection schemes available which aim to remedy the above problems. Our approach for OM3 employs a scheme ported to MOM4.0 from the MIT GCM[5]. The scheme is based on a third order upwind biased approach of Hundsdorfer and Trompert (1994) who employ the flux limiters of Sweby (1984). This implementation of numerical advection is non-dispersive, preserves shapes in three dimensions, and precludes tracer concentrations from moving outside of their natural ranges. The scheme is only modestly more expensive than Quicker, and it does not signficantly alter the simulation relative to Quicker in those regions where the flow is well resolved.

sures less than 5500 db, and freezing to 12°C for pressures greater than 5500 db.

[5]We thank Alistair Adcroft for assistance with this work. The online documentation of the MIT GCM at http://mitgcm.org contains useful discussions and details about this advection scheme.

Hence, we have found it to be an essential element of the ocean climate model.

2.7. Penetrative shortwave radiation

The absorption of solar shortwave radiation within the upper ocean varies significantly in both space and time. High levels of chlorophyll result in almost all sunlight being absorbed within just a few meters of the ocean surface in biologically productive waters such as near the equator, in coastal upwelling zones, and polar regions. In contrast, low chlorophyll levels in subtropical gyres allow solar radiation to penetrate with an e-folding depth (in the blue-green part of the visible spectrum) of 20–30 m.

In ocean climate models with thick upper grid cells (e.g. 50 m), the geographic variation of shortwave penetration is unimportant since all shortwave radiation is generally absorbed within this single box. In OM3, however, the top box is 10m with a resting ocean free surface. Up to 20% of incoming solar radiation can penetrate below this level in many regions of the ocean. Without allowing shortwave radiation to penetrate, radiative heating would overly heat the top cell, causing its temperature to grow well above observed. One way to address this problem is to allow shortwave penetration with a given e-folding depth that is constant in space and time. However, for long term global climate simulations, we believe it is important to allow geographical and seasonal variations of the shortwave penetration. Shy of a prognostic biological model, we choose a climatology rather than a global constant.

Sweeney et al. (2005) compile a seasonal climatology of chlorophyll based on measurements from the NASA SeaWIFS satellite. They used this data to develop two parameterizations of visible light absorption based on the optical models of Morel and Antoine (1994) and Ohlmann (2003). The two models yield quite similar results when used in global ocean-only simulations, with very small differences in heat transport and overturning. We use the Sweeney et al. (2005) chlorophyll climatology in CM2.0 and CM2.1 along with the optical model of Morel and Antoine (1994). Although the chlorophyll climatology remains unchanged even when considering changes in radiative forcing due to anthropogenic greenhouse gas changes, we believe it is a far better

means of parameterizing shortwave penetration than available with a global constant e-folding depth. Future earth system models possessing prognostic biogeochemistry will be better able to represent potential changes in chlorophyll, and hence radiative penetration, under changing climates.

2.8. Background vertical mixing coefficients

Vertical tracer diffusion plays a major role in determining the overall structure of the ocean circulation, as well as its impact on climate (Bryan, 1987; Park and Bryan, 2000). Direct estimates based on measurements of temperature microstructure and the diffusion of passive tracers (Ledwell et al., 1993) indicate that the diffusivity is on the order of $0.1-0.15\times10^{-4}\,\mathrm{m^2\,s^{-1}}$ in the extra-tropical pycnocline, and Gregg et al. (2003) indicate yet smaller values near the equator. In the deep ocean, both basin-scale budget studies (Whitehead and Worthington, 1982) and direct measurements (Toole et al., 1994, 1997; Polzin et al., 1996, 1997) indicate that diffusivities are on the order of $1-2\times10^{-4}\,\mathrm{m^2\,s^{-1}}$.

Until recently, most ocean climate models were unable to match the low level of diapycnal diffusivity within the pycnocline suggested from the microstructure and tracer release measurements. The reason they had problems is that some models included high values of spurious diapycnal diffusion associated with the horizontal background diffusion required to stabilize earlier versions of the neutral diffusion scheme (Griffies et al., 1998), and some had large diapycnal diffusion associated with upwind advection (Maier-Reimer et al., 1983). Additionally, earlier GFDL models followed Bryan and Lewis (1979) and used a vertical diffusivity of $0.3\times10^{-4}\,\mathrm{m^2\,s^{-1}}$ in the upper ocean and $1.3\times10^{-4}\,\mathrm{m^2\,s^{-1}}$ in the deep ocean. Higher levels of vertical diffusion within the thermocline result in an increase in tropical upwelling and poleward heat transport in both hemispheres (Gnanadesikan et al., 2003) which may compensate for the relative sluggishness of boundary currents in the coarse models.

In OM3, we maintain a relatively refined vertical resolution in the upper ocean, largely to allow for a realistically small vertical diffusivity within the tropical thermocline. Mod-

elling experience indicates a strong sensitivity of the equatorial current structure and ENSO variability to the levels of tracer diffusion, with realistic simulations requiring small values consistent with the observations (Meehl et al., 2001).

Simmons et al. (2004) illustrate the utility of including a parameterization of mixing associated with breaking internal waves arising from the conversion of barotropic to baroclinic tidal energy. Such wave breaking occurs especially above regions of rough bottom topography (Polzin et al., 1997). The results from the Simmons et al. (2004) simulations indicate that a small value through the pycnocline and larger value at depth, qualitatively similar to the profile of Bryan and Lewis (1979), is far better than a vertically constant diffusivity.

While the Simmons et al. (2004) work remains the subject of much research, we decided to maintain the approach of Bryan and Lewis (1979) by prescribing a flow independent background diffusivity for OM3. To reflect the observations noted above, we modified the canonical Bryan and Lewis (1979) values to the smaller levels of $0.1\times10^{-4}\,\mathrm{m^2\,s^{-1}}$ in the upper ocean and $1.2\times10^{-4}\,\mathrm{m^2\,s^{-1}}$ in the deeper ocean within the tropics. In the high latitudes, although not suggested from observations, we used the larger value of $0.3\times10^{-4}\,\mathrm{m^2\,s^{-1}}$ in the upper ocean. Figure 7 shows the vertical profile of background vertical tracer diffusivity.

Figure 8 shows effects on the North Atlantic sea surface salinity (SSS) in CM2.0 arising from increased Bryan-Lewis vertical diffusivity in the high latitudes. Increased mixing reduced the global rms error in the coupled model from 0.84 to 0.79, and in the North Atlantic from 1.57 to 1.41. The main goal of the increased tracer diffusion in the high latitudes was not necessarily to reduce the SSS biases by this modest level. Rather, it was to address a model bias in the subpolar North Atlantic towards weak Labrador Sea deepwater formation, and a perceived fragility of simulated Atlantic overturning. In retrospect, this ocean bias was largely associated with the equatorial shift of the wind stress in the atmospheric model discussed in Sect. 1.3 and more fully in Delworth et al. (2005). Consequently, the enhanced vertical tracer diffusivity likely was unneeded in CM2.1 where the finite volume atmospheric model does not

have an equatorial bias. Indeed, the overturning circulation is quite vigorous in CM2.1 (Delworth et al., 2005). Limitations in resources and time precluded our re-tuning the vertical diffusivity in CM2.1.

Many modelers have traditionally taken a Prandtl number (ratio of viscosity to diffusivity) on the order 1–10. In OM3, we choose a depth independent background vertical viscosity of $10^{-4}\,m^2\,s^{-1}$. The level of background viscosity can also affect the equatorial currents, as discussed in Large et al. (2001). There is no theoretical or observational justification for this value of the vertical viscosity.

2.9. Surface ocean boundary layer

In addition to the background vertical diffusivity and viscosity discussed in Sect. 2.8, we use the parameterization of boundary layer mixing proposed by Large et al. (1994). This k-profile parameterization (KPP) scheme prescribes added levels of tracer and velocity mixing in regions where mixing is likely to be under-represented in this hydrostatic model, such as in the important surface ocean boundary layer. The KPP scheme has been used by many climate models during the past decade. It provides a suitable framework within which to consider various mixing processes.

Beyond the standard settings recommended by Large et al. (1994), interior mixing in OM3 is enhanced by double diffusion due to salt fingering and diffusive convection. These processes occur in regions where the vertical temperature and salinity gradients have the same sign, and so contribute oppositely to the vertical density gradient (see Schmitt, 1994; Toole and McDougall, 2001; Kantha and Clayson, 2000, for reviews of these processes). Additionally, the Richardson number computation is modified by adding to the resolved vertical shear an unresolved shear due to tidal velocities diagnosed from a tide model according to the methods discussed in Lee et al. (2005). These tidal velocities are significant near coastal regions (see Fig. 9), in which case the Richardson numbers are small thus enhancing the vertical mixing coefficients. We found this extra mixing to be especially useful in certain river mouths to assist in the

horizontal spreading of river water into the ocean basins by the horizontal currents.

3. Novel methods and some lessons learned

The purpose of this section is to highlight numerical and physical features of the ocean climate model that are either novel or where novel insights and experiences were garnered.

3.1. Ocean free surface and freshwater forcing

Variations in the ocean free surface are precluded in models using the rigid lid approximation of Bryan (1969a). This approximation was commonly made in early climate models for computational expendiency since it filters out fast barotropic undulations of the ocean free surface. However, as noted by Griffies et al. (2001), rigid lid models exhibit poor computational efficiency on parallel computers. The reason is that the elliptic problem associated with the rigid lid involves global communication across all parallel computer processors. This type of communication is costly on machines using a distributed computer processor architecture (i.e. the machines typically used for global climate modelling). Explicit free surface methods only involve less costly local processor communication, which generally leads to a far more efficient algorithm.

There are physical consequences that must be considered when making the rigid lid approximation. First, the rigid lid distorts the dispersion relation for planetary waves, especially those waves with spatial scales on the order of the barotropic Rossby radius (thousands of kilometers). Second, as commonly implemented in ocean climate models, the rigid lid precludes the transport of water across ocean boundaries. The reason is that the volume of all grid cells is fixed in time, thus precluding transport of water across ocean boundaries. Hence, there is no barotropic advection giving rise to the Goldsborough-Stommel circulation, and freshwater dilution of tracer concentrations must be parameterized (see Huang, 1993; Griffies et al., 2001, and references therein

for more thorough discussion of these issues).

The ocean's density, and hence its pressure and circulation, are strongly affected by the transport of water across the ocean boundaries via evaporation, precipitation, river runoff, and ice melt. That is, ocean boundaries are open to water fluxes, and these fluxes are critical to ocean dynamics. Additional climatologically important tracers, such as dissolved inorganic carbon, are also affected by water transport, as is the ocean's alkalinity. "Virtual salt fluxes" used in fixed volume ocean models aim to parameterize the effects of boundary water transport on the density field. Such models transport salt, rather than water, across the air-sea interface. However, only a neglible amount of salt crosses Nature's air-sea interface. Additional virtual fluxes are required in constant volume models for other tracers. In general, virtual tracer flux methods can distort tracer changes, such as in the climatologically important situation discussed below where salinity is low as near river mouths.

Free surface methods, such as the one proposed by Griffies et al. (2001) and Griffies (2004) render the ocean volume time dependent. A time dependent ocean volume opens ocean boundaries so that water can be exchanged with other parts of the climate system. Such water transport across boundaries manifests as changes in ocean surface height (see equation (32)). When formulated in this way, virtual tracer fluxes are inappropriate. Free surface methods also remove the distortion of barotropic planetary waves since they allow for time dependent undulations of the ocean's free surface.

Although most ocean climate models today employ a free surface, tracer budgets in many models still assume the ocean volume is constant. That is, they do not allow water to be exchanged with other parts of the climate system. We therefore find it interesting to consider how the response of salinity to a freshwater perturbation differs in a model that uses virtual tracer fluxes from a model allowing water to cross its boundaries. For this purpose, consider an ocean comprised of a single grid cell affected only by surface freshwater fluxes. Conservation of salt in a Boussinesq model leads to

$$\partial_t (h\, s) = 0 \tag{2}$$

where h is the cell's vertical thickness and s is the salinity. In a model whose volume

can change, the thickness of the ocean is altered by the addition of freshwater via

$$\partial_t h = q_w \tag{3}$$

where $q_w = P - E + R + I$ is the volume per horizontal area per time of precipitation, evaporation, river runoff, and ice melt that crosses the ocean surface (Eq. 25 in the appendix). In this case, salinity evolves according to

$$h\,\partial_t s = -s\,q_w . \tag{4}$$

For example, freshwater input to the ocean ($q_w > 0$) dilutes the salt concentration and so reduces salinity.

In a model using a fixed volume, salinity evolves according to

$$h\,\partial_t s = -s_{\text{ref}}\,q_w , \tag{5}$$

where now h is time independent, and s_{ref} is a constant salinity needed to ensure that total salt is conserved in the constant volume model assuming fresh water is balanced over the globe[6]. The virtual salt flux is given by

$$F^{(\text{virtual salt})} = s_{\text{ref}}\,q_w . \tag{6}$$

Models have traditionally taken $s_{\text{ref}}=35$, as this is close to the global averaged salinity in the World Ocean.

Use of a global constant normalization distinguishes the salinity budget (Eq. 5) in the virtual salt flux model from the local salinity used in a model that exchanges water with its surroundings (Eq. 4). To illustrate how this factor alters the salinity response to freshwater forcing, consider a case where fresh river water is added to a relatively

[6]Total salt is not conserved in constant volume models using the salinity Eq. (4) appropriate for real freshwater flux models. Nonetheless, attempts have been made at GFDL to run constant volume models with the salinity Eq. (4) in an aim to properly simulate the local feedbacks on salinity from freshwater. Unfortunately, such models tend to have unacceptably large drifts in salt content and so have not been used at GFDL for climate purposes.

fresh ocean region where $s<s_{ref}$ (e.g. rivers discharging into the Arctic Ocean). Here, since the actual local salinity is fresher than the globally constant reference salinity, the dilution effect in the virtual salt flux model will be stronger than the real water flux model. Such overly strong feedbacks can introduce numerical difficulties (e.g. advection noise and/or salinity going outside the range allowable by the equation of state) due to unphysically strong vertical salinity gradients. For OM3, we have found problems with overly fresh waters to be particularly egregious in shallow shelf areas of the Siberian Arctic. For the opposite case where evaporation occurs over salty regions with $s>s_{ref}$ (e.g. evaporation over subtropical gyres), the virtual salt flux model underestimates the feedbacks onto salinity.

We now illustrate how the use of virtual salt fluxes alter the simulation characteristics in the coupled climate model relative to real water fluxes. For this purpose, we ran two CM2.1-like climate models for a short period of time. In the standard CM2 experiments, water is input as a real water flux that affects the surface height by adding volume to the ocean fluid. For the purpose of comparison with a virtual salt flux run, we insert river water just into the top model grid cell[7]. We ran a second experiment with virtual salt fluxes where the virtual salt fluxes associated with the river water are applied over the top cell. Consistent with the previous theoretical discussion, results in Fig. 10, taken in August of the second year, show that the virtual salt flux model has systematically fresher water near river mouths, with largest differences around 14 psu fresher. Away from rivers, the differences are minor, and consistent with variability. The virtual salt flux experiment became numerically unstable in October of the second year due to extremely unphysical values of the salinity, whereas the real water flux experiment remained stable.

In conclusion, virtual tracer fluxes can do a reasonable job of parameterizing the effects of freshwater on tracer concentration in regions where the globally constant reference tracer concentration is close to the local concentration. However, for realistic

[7] In the standard CM2 experiments, river water is inserted throughout the upper 40m of the water column in a manner described in Sect. 3.6.

global climate models, local concentrations can deviate significantly from the global reference, especially near river mouths. This deviation compromises the physical realism and numerical stability of the simulation. These are the key reasons that we jettisoned virtual tracer fluxes in our standard climate model simulations in favor of allowing water fluxes to cross the ocean model boundaries[8].

3.2. Time stepping the model equations

As noted by Griffies et al. (2000a), the leap frog remains the most commonly used method for discretizing the time tendency in primitive equation ocean climate models. OM3.0 retains this approach. However, an alternative time stepping scheme was developed for OM3.1. This time staggered method has much in common with that used in HIM (Hallberg, 1997) as well as the MIT GCM (Marshall et al., 1997; Campin et al., 2004). Details of the scheme are provided in Chapter 12 of Griffies (2004). We introduce the main features here since the scheme possesses some highly favorable characteristics of use for ocean climate modelling. We also illustrate sensitivity of the simulation to the time stepping algorithm by comparing model integrations with the leap frog to the time staggered scheme.

3.2.1. Characteristics of staggered time stepping

Leap frog tendencies lead to time splitting which necessitates the use of time filtering (e.g. Haltiner and Williams, 1980; Durran, 1999). Filters reduce the second order accurate leap frog to first order (Durran, 1999). Additionally, when realized with an undulating free surface as in OM3, Griffies et al. (2001) showed how time filters make it nontrivial to satisfy the constraints of both local and global tracer conservation. Local conservation means that a uniform tracer concentration remains unchanged in the

[8]The impact of virtual salt fluxes on forcing of the meridional overturning circulation in the North Atlantic is currently under investigation by researchers at GFDL (Ron Stouffer, personal communication).

absence of boundary tracer fluxes even in the presence of momentum fluxes. Global conservation means that boundary tracer fluxes are precisely balanced by changes in tracer content in the full model domain. Both forms of conservation are important for earth system modelling.

The new scheme discretizes time tendencies with a forward time step. Second order accuracy is maintained by staggering tracer and velocity fields by one-half time step in a manner analogous to spatial staggering on Arakawa grids. We therefore refer to this method as a staggered scheme[9]. As forward time stepping schemes do not admit time splitting modes, no time splitting mode exists, and so no time filters are needed. The new scheme therefore ensures both local and global tracer conservation.

Temporal stability of the staggered scheme is twice that of the leap frog in cases where the model's time step is constrained by either gravity waves or dissipation. To understand this very important practical result, recall that the leap frog updates the ocean state by a $\Delta\tau$ time step, yet it employs $2\Delta\tau$ for the tendency calculation. Hence, gravity waves and dissipative operators (i.e. diffusion, friction, and upwind biased advection) have stability properties based on $2\Delta\tau$. The staggered scheme updates the ocean state by $\Delta\tau$ and it employs $\Delta\tau$ to compute tendencies. Hence, its stability properties are based on the $\Delta\tau$ time step.

Preliminary analysis of the leap frog version OM3.0 reveals that its time step is largely constrained by friction along the equatorial region within the western boundaries, especially in the Indonesian region. Hence, the above stability result indicates that OM3.1 should be stable with twice the time step using the staggered scheme as required for the leap frog. Indeed, this is the case. That is, when OM3.0 is stable with the leap frog scheme using a time step $\Delta\tau_{\text{leap}}$, OM3.1 has been found to be stable using the

[9]We retain second order centered differencing for the velocity advection, thus prompting the use of an Adams-Bashforth method to time discretize this term (Durran, 1999). We chose the temporally third order accurate scheme for this purpose due to its enhanced stability properties over the second order scheme.

staggered scheme with twice the time step

$$\Delta\tau_{\text{stag}} = 2\Delta\tau_{\text{leap}}. \tag{7}$$

Consequently, the computational cost of OM3.1 with the staggered scheme is one-half that of OM3.0 which uses the leap frog scheme.

To illustrate the time staggered method, it is sufficient to consider an update of thickness weighted tracer (see Sect. 19 for discussion of the tracer equation). With a leap frog discretization of the time tendency, we compute

$$\frac{(hT)^{\tau+\Delta\tau_{\text{leap}}} - (\overline{h}\,\overline{T})^{\tau-\Delta\tau_{\text{leap}}}}{2\,\Delta\tau_{\text{leap}}} =$$

$$-\nabla\cdot[\,(h\,\mathbf{u})^{\tau}\,T^{\tau-\Delta\tau_{\text{leap}}} + h^{\tau}\,\mathbf{F}^{\tau-\Delta\tau_{\text{leap}}}\,] - \delta_k\,[\,w^{\tau}\,T^{\tau-\Delta\tau_{\text{leap}}} + F_z^{\tau+\Delta\tau_{\text{leap}}}\,], \tag{8}$$

where $\overline{h}$ and $\overline{T}$ are the time filtered values of the tracer cell thickness and concentration, $(\mathbf{u}, w)$ are the advection velocity components, $(\mathbf{F}, F_z)$ are the SGS fluxes, ∇ is the horizontal gradient operator, and δ_k is the vertical finite difference operator. Note that the vertical SGS flux component F_z is evaluated implicitly in time, and the advective fluxes are computed assuming an upwind biased scheme so that the tracer concentration is lagged in time just as the horizontal SGS flux (e.g. Holland et al., 1998; Pacanowski and Griffies, 1999). The time time staggered form of the discrete tracer equation is given by

$$\frac{(hT)^{\tau+\frac{1}{2}\Delta\tau_{\text{stag}}} - (hT)^{\tau-\frac{1}{2}\Delta\tau_{\text{stag}}}}{\Delta\tau_{\text{stag}}} =$$

$$-\nabla\cdot[\,(h\,\mathbf{u})^{\tau}\,T^{\tau-\frac{1}{2}\Delta\tau_{\text{stag}}} + h^{\tau}\,\mathbf{F}^{\tau-\frac{1}{2}\Delta\tau_{\text{stag}}}\,] - \delta_k\,[\,w^{\tau}\,T^{\tau-\frac{1}{2}\Delta\tau_{\text{stag}}} + F_z^{\tau+\frac{1}{2}\Delta\tau_{\text{stag}}}\,]. \tag{9}$$

Except for the time filtering applied to the leap frog method, the two Eqs. (8) and (9) are identical when $\Delta\tau_{\text{stag}}=2\Delta\tau_{\text{leap}}$. However, no time steps are skipped when computing discrete time tendencies with the time staggered method, since this approach employs

forward time differences. No time filtering is therefore needed in this approach. In effect, the time staggered method stays on just one of the two leap frog branches. This is the fundamental reason that the staggered method should be expected, for many purposes, to yield similar solutions to the leap frog yet at half the computational cost.

3.2.2. Implicit and semi-implicit terms

As with many other ocean climate models, we time step the vertical physical processes (i.e. vertical diffusion and vertical friction) with an implicit time step. In the staggered method, the implicit portion leads the explicit portion by a single time step, whereas the implicit leads by two time steps with the leap frog. The staggered scheme is thus more accurate for the vertical implicit processes.

In the velocity equation, we implement the Coriolis force semi-implicitly (Eq. 21). This method is second order accurate, which is shared by a time explicit implemention. We prefer the semi-implicit method as it provides some added stability in practice. Although the model's baroclinic time step is well within the range needed to resolve inertial oscillations, extra stability is useful to suppress an inertial instability of the coupled ocean and sea ice system[10]. Note that inertial energy is quite strong in the coupled model since the atmosphere and land models have a diurnal cycle whereby the atmospheric and sea ice fields felt by the ocean (stress, fresh water, turbulent and radiative fluxes) are updated every 3 h[11]. Inertial energy has important contributions to the mixing coefficients determined by the model's boundary layer scheme (Sect. 2.9).

3.2.3. Sensitivity to the time stepping scheme

During the bulk of our development process, the ocean model employed the leap frog scheme for the tracer, baroclinic, and barotropic equations. However, upon develop-

[10] The precise mechanism of this instability is under investigation.

[11] As recommended by Pacanowski (1987), wind stress applied to the ocean surface is computed using the relative velocity between the atmospheric winds and the ocean currents.

ing the staggered time stepping scheme for the tracer and baroclinic equations, and a predictor-corrector for the barotropic equations (Killworth et al., 1991), we became readily convinced that the new time stepping schemes were better from both fundamental numerical and practical model efficiency perspectives. The question arose whether switching to the new time stepping schemes would require retuning of the physical parameterizations.

Preliminary tests were run with the ocean and ice models using an annually repeating atmospheric forcing with daily synoptic variability, again repeating annually. Runs using the new time staggered scheme had a 2 h time step for both tracer and baroclinic momentum, and a predictor-corrector scheme (e.g. Killworth et al., 1991; Griffies, 2004) for the barotropic equations with a 90 s time step. We prefer the predictor-corrector for the barotropic equations due to its increased stability relative to the leap frog, as well as its ability to dissipate grid scale noise commonly found when simulating gravity waves on a B-grid (Killworth et al., 1991; Griffies et al., 2001). The comparison was made to a leap frog ocean using 1 h time steps for the tracer and baroclinic equations, and (3600/64) s for the leap frog barotropic equations.

Analysis of these solutions after 10 years revealed that regions with high frequency temporal variability, such as the equatorial wave guide, exhibit the most differences instantanously. Figure 11 illustrates the situation along the equator in the East Pacific. The leap frog simulation exhibits substantial splitting behaviour, even with a nontrivial level of time filtering from a Robert-Asselin filter (Haltiner and Williams, 1980; Durran, 1999) aiming to suppress the splitting. Moving just 5° N of the equator, however, reveals that the simulation has much less relative variability, and a correspondingly negligible amount of time splitting. Even though the simulation along the equator showed substantial time splitting, over time the large scale patterns and annual cycles showed negligible differences between time stepping schemes. Time averaging, even over just a day, seems sufficient to smooth over most of the instantaneous differences.

Tests were then run with CM2.0 and CM2.1. Instantaneous differences were much larger, as expected due to the nontrivial natural variability in the coupled system with

a freely evolving atmosphere. Nonetheless, differences for large scale patterns and seasonal or longer time averages were within levels expected from the model's natural variability.

Differences do occur due to (1) different barotropic time schemes, (2) third order Adams-Bashforth for momentum advection, (3) differences in implicit physics, (4) Robert-Asselin filtering in the leap frog scheme. But to the extent that the solution is dominated by geostrophically balanced flow, the time stepping schemes should produce similar results. It is pleasantly surprising that the solutions maintain close correspondence even in the equatorial region and in regions of strong deep convection.

Although our tests revealed only minor differences between the two time stepping schemes, we believe the analysis and results in this section provide compelling reasons to eschew leap frog time schemes for ocean climate modelling. Troubles realizing tracer conservation create difficulty when integrating for centuries, or when developing new component models such as biogeochemical or ecosystem models. We conjecture that the small differences noted in our tests will accumulate on the centennial and longer time scales, although we are not prepared to run the coupled model to rigorously test the level to which the solutions drift apart.

3.2.4. Comments on time stepping schemes

In general, the leap frog time splitting mode is very unsatisfying from a fundamental numerical perspective. Furthermore, the practical bottomline is that the conservative staggered scheme is about twice as stable as the leap frog scheme. These conclusions are likely unsurprising to those familiar with the computational fluid dynamics literature (e.g. Durran, 1999), where leap frog methods have long since been abandoned. However, as documented by Griffies et al. (2000a), the majority of ocean climate models still use the leap frog, with the notable exception of Hallberg (1997), Marshall et al. (1997), and Campin et al. (2004). We believe the GFDL model documented in this paper is the only model contributing to the Fourth IPCC assessment that does not use a leap frog based method. As shown here, alternative methods can provide a straightforward

means to move beyond leap frog within the current class of climate models, with the potential to reduce the model cost by one half and to conserve tracer to within machine precision.

3.3. Neutral physics

During the past few decades, tracer studies have shown that much of the ocean's large scale lateral transport processes are oriented according to local isopycnal directions, also known as "neutral" directions (e.g. McDougall, 1987), rather than surfaces of constant geopotential. Respecting this orientation has motivated the use of rotated diffusive parameterizations by Solomon (1971), Redi (1982), Olbers et al. (1985), and McDougall and Church (1986). Subsequent work by Gent and McWilliams (1990) and Gent et al. (1995) promoted the additional notion of eddy-induced advective processes (or equivalently, eddy induced skew diffusive processes). The numerical realization of these ideas in many present day z-models, including OM3, follows Griffies et al. (1998) and Griffies (1998). Generically, we refer to these processes as "neutral physics". The purpose of this section is to explain how neutral physics appears in OM3.0 and OM3.1

The use of neutral physics in z-models can alter the simulation in nontrivial ways. First, it significantly reduces the unphysically large level of spurious cross isopycnal (i.e. dianeutral) mixing encountered in the older models using horizontal diffusion[12]. Reducing spurious mixing greatly improves the simulation's physical integrity, and so these schemes are ubiquitous in the ocean models participating in AR4. Use of the schemes also greatly affects the thermocline structure (Danabasoglu et al., 1994; Gnanadesikan,

[12]Nontrivial problems remain for z-model simulations using resolutions admitting vigorous mesoscale eddies. In this case, eddies pump tracer variance to the grid scale. It has been found empirically that this variance is cannot be dissipated using traditional methods without incurring significant levels of spurious dianeutral mixing (Roberts and Marshall, 1998; Griffies et al., 2000b). It remains for z-modelers to empirically prove that their mesoscale eddying simulations can integrate over climatologically relevant time scales (centuries) without incurring unacceptable levels of spurious mixing.

1999a), heat transport (Gnanadesikan et al., 2003) and the distribution of biologically active tracers (Gnanadesikan, 1999b,c; Gnanadesikan et al., 2002).

In the following we discuss various aspects of the neutral physics as implemented in CM2.0 and CM2.1. For this purpose it is useful to refer to equation (30) which provides an expression for the tracer fluxes arising from neutral physics.

The neutral diffusive aspects of OM3.0 and OM3.1 differ. For OM3.0 we take the along isopycnal (i.e. the neutral) diffusivity A_l to be the same depth-independent function of the flow as the skew-diffusivity to be described later in this section. This setting is traditional in ocean models, as it is thought that the neutral diffusive and skew diffusive elements of the SGS transport arise from the same mesoscale eddies. However, for OM3.1 we set the neutral diffusivity to the constant value of A_l=600m^2 s^{-1}. This change was motivated primarily to reduce biases in the North Pacific sea ice extent found in CM2.1, where sea ice was found to have far too large an extent in the coupled simulations. In this region, isotherms and neutral directions deviate substantially. Hence, although this change in tracer mixing was not based on fundamental physical reasoning, increasing the neutral diffusivity in OM3.1 moves more heat horizontally, which reduced the overly broad sea ice extent. We illustrate these effects in Fig. 12.

For both OM3.0 and OM3.1, in regions where the neutral slope (Eq. 31) steepens, such as near the upper ocean boundary layer and within convective regions, neutral diffusion is exponentially converted to horizontal diffusion. The exponential tapering is prescribed according to the methods in Appendix B of Large et al. (1997), with our tapering started as the neutral slope becomes steeper than 1/500. Tapering also occurs in regions where the slope is less than 1/500 in regions where unresolved eddies are thought to be partially cutoff because of their proximity to the ocean surface (Treguier et al., 1997; Held and Schneider, 1999). Again, the prescription given by Large et al. (1997) is followed. The region where tapering is employed is termed the neutral boundary layer in the following.

Treatment of the skew-diffusive aspect of neutral physics in the neutral boundary layer is different from neutral diffusion. Here, the quasi-Stokes transport $-A_{gm}\,\mathbf{S}$ (Mc-

Dougall and McIntosh, 2001; Griffies, 2004) is linearly tapered to zero starting from the boundary layer base where the magnitude of the slope **S** in either horizontal direction is just greater than 1/500. A similar method was suggested by Treguier et al. (1997) and Greatbatch and Li (2000). Because the quasi-Stokes transport is a linear function of depth within the boundary layer, the horizontal eddy velocity $\mathbf{u}^* = -\partial_z (A_{gm}\,\mathbf{S})$ is vertically constant in this region, with a magnitude inversely proportional to the boundary layer depth. A generally nontrivial vertical shear in $\mathbf{u}^*$ is seen at the base of the boundary layer, and it is oriented in a manner to ensure the reduction of potential energy even in regions where the slope is vertical (see Sect. 15.3 of Griffies, 2004, for details)[13].

Our choice of 1/500 for the maximum slope parameter $S_{\max}$ is notably smaller than the more commonly used 1/100 or larger. Our reasoning for choosing this value is as follows. The diffusivity times the maximum slope represents a maximum volume flux associated with the Gent and McWilliams (1990) parameterization. This product determines an upper limit on what parameterized eddies can do in countering wind-driven Ekman fluxes. Given that Ekman volume fluxes are of order $1\,\mathrm{m}^2\,\mathrm{s}^{-1}$, we chose not to let the parameterized fluxes greatly exceed this value. The maximum skew diffusivity used in OM3 experiments is $600\,\mathrm{m}^2\,\mathrm{s}^{-1}$, which motivated taking a maximum slope on the order of 1/500 rather than the larger 1/100.

The mixed layer depth is particularly sensitive to $S_{\max}$. Figures 13a and 13b show mixed layer depth differences between a run with $S_{\max}$=1/100 and another with $S_{\max}$=1/500. The smaller $S_{\max}$ simulation generally results in decreased mixed layer depth, particularly in the Southern Hemisphere mode water formation regions and in the Labrador Sea. This behaviour illustrates how details in the neutral physics parameterization interact with the mixed layer, and thus can have a nontrivial impact on the potential vorticity structure of the mode and intermediate waters.

[13]To ensure proper orientation of the eddy velocity, it is important to maintain a non-negative squared buoyancy frequency. For this purpose, we apply the convective adjustment scheme of Rahmstorf (1993) subsequent to vertical diffusion in order to ensure that no unstable regions are acted on by the neutral physics scheme.

The overturning streamfunction associated with the quasi-Stokes transport from Gent and McWilliams (1990) is also sensitive to the value of $S_{\max}$. As seen in Figs. 13c and 13d this overturning is dominated by the eddy return flow which, to some extent, cancels the Deacon cell (Marshall et al., 1993; Karoly et al., 1997; Hallberg and Gnanadesikan, 2001). This circulation is much stronger when $S_{\max}=1/100$ than $S_{\max}=1/500$. Interestingly, it appears to be stronger because the slopes in the ACC are steeper. The reasons for this are beyond the scope of this paper. Taken together, these results illustrate that not only the value of the diffusion coefficient, but details of how this coefficient is tapered for large slopes, can produce significant changes in the large-scale circulation. This fact should be remembered when considering the impact of the Gent and McWilliams (1990) scheme in different models.

There are many methods to prescribe the diffusivity A_{gm} used in the neutral physics schemes. Griffies (2004) summarizes the proposals, such as Held and Larichev (1996) and Visbeck et al. (1997), that derive a depth independent diffusivity determined as a function of vertically integrated flow properties. In the construction of OM3, we tested schemes which suggest that the length scale for the diffusivity be set by the Rossby radius (Stone, 1972; Stammer, 1997; Bryan et al., 1999; Smith and Vallis, 2002). However, they generally produced far too large diffusivities within the equatorial region of the model. As this is the region of OM3 with the most refined resolution, we wish to use a tropical diffusivity that is small in order to admit flows dominated by advective, not subgrid scale, processes.

The method used in OM3 is based on setting the diffusivity proportional to the vertically averaged baroclinicity

$$A_{gm} = \alpha \overline{|\nabla_z \rho|}^{z} \left(\frac{L^2 g}{\rho_o N_o} \right) . \tag{10}$$

Here, α is a dimensionless tuning constant set to 0.07, L is a constant length scale set to 50km, N_o is a constant buoyancy frequency set to $0.004\,\mathrm{s}^{-1}$, $g=9.8\,\mathrm{m\,s}^{-1}$ is the acceleration of gravity, $\rho_o=1035\,\mathrm{kg\,m}^{-3}$ is the reference density for the Boussi-

nesq approximation, and $\overline{|\nabla_z \rho|}^z$ is the average of the horizontal density gradient (i.e. the baroclinicity) taken over the depth range 100 m to 2000 m (this depth range was originally suggested by Treguier et al., 1997). A five year mean of this diffusivity from CM2.1 is shown in Fig. 14. The largest values are found in the boundary currents as well as the Antarctic Circumpolar Current. These are generally the regions where it is expected that eddy transport effects are the largest. Much smaller values are found outside these regions, as well as in the tropics. The smaller values in these regions allow for the advective dynamics resolved by the simulation to dominate the subgrid scale parameterization. Although this diffusivity has been found to be suitable for our purposes, it is unsatisfying that we cannot justify it from theory. Thorough comparisons with alternatives remain to be conducted to clarify the utility of this approach.

As noted by Gerdes et al. (1991), truncation errors with the discrete neutral physics schemes, such as those of Griffies et al. (1998) and Griffies (1998), can cause tracer concentrations to move outside their physical bounds. This problem is similar to that arising with numerical advection schemes. To address this problem with neutral physics, Beckers et al. (1998, 2000) propose the use of flux limiters. We have not implemented neutral physics flux limiters in MOM4.0. Instead, we took a far less sophisticated approach. Here, if the tracer concentration at a point moves outside a user specified range, the tracer fluxes neutral physics reduce those from horizontal diffusion. Horizontal diffusive fluxes have been found to be needed only in special places, mostly in the high latitudes near sea ice edges and/or land/sea boundaries. Relatedly, because of the problems with truncated neutral physics grid stencils next to the solid earth and surface boundaries, we reduced neutral physics to horizontal diffusion at grid points adjacent to all boundaries. This approach was also recommended by Gerdes et al. (1991).

3.4. Horizontal friction

The ubiquitous use of horizontal friction in global ocean climate models is not motivated from fundamental physical principles. Instead, horizontal friction provides a numerical closure. In particular, it is used to maintain a modest grid Reynolds number[14] and to resolve boundary currents (Griffies and Hallberg, 2000; Large et al., 2001; Smith and McWilliams, 2003; Griffies, 2004). In effect, modelers choose horizontal friction to be the smallest available given the model grid resolution and subjective notions of what constitutes a noisy simulation and/or under-resolved boundary currents. The work of Griffies et al. (2000b) also noted that simulations with under-resolved boundary currents in z-models can be associated with unphysically large levels of spurious dianeutral tracer mixing. Such problems can cause egregious loss of water mass integrity in climate simulations. Hence, it is important to balance the desires of running a model using very low friction with the conflicting needs of ensuring that admitted flow features are well represented.

Large et al. (2001) and Smith and McWilliams (2003) introduced a novel method to reduce the model's horizontal friction while satisfying the numerical needs mentioned above. Their " anisotropic viscosity" scheme has been employed in OM3 within the equatorial band from 20° S to 20° N. Consistent with Large et al. (2001), the tropical current structures in OM3 are far more vigorous, and realistic, relative to the older isotropic method, and the numerical integrity of the solution is maintained (i.e. flow features are well represented, thus ensuring a negligible level of noise). Notably, the orientation of the viscosity in this region is set according to the coordinate grid lines, as suggested by Large et al. (2001). This approach ensures that larger meridional values are next to western boundaries (to resolve the Munk boundary layer) and larger zonal values are closer to the equator (to maintain a modest grid Reynolds number in the presence of strong zonal currents). Because the meridional viscosities are very small

[14]The grid Reynolds number is $\mathrm{Re}=U\,\Delta/A$, where U is the speed of the currents, Δ is the grid scale, and A is the viscosity.

within the equatorial region, the equatorial current structures remain tight with speeds reaching to the observed 1 m s^{-1}. More on the equatorial current structure is discussed in Wittenberg et al. (2005).

Figure 15 shows the time independent zonal and meridional viscosities used in OM3.0 and OM3.1 at the ocean surface. Smaller viscosities are used at depth according to the profile suggested by Large et al. (2001). Outside of the tropics, the viscosity reverts to the traditional isotropic method, with a grid size dependent and vertically constant background viscosity added to a horizontal shear dependent Smagorinsky viscosity (Smagorinsky, 1963, 1993; Griffies and Hallberg, 2000). The Smagorinsky contribution is most noticeable in strong shear regions such as the western boundaries, but for the most part it is sub-dominant to the larger background viscosity shown in these figures. Additionally, to suppress a coupled ocean and sea ice instability associated with frictional CFL violations, we reduced the isotropic friction by 2/3 poleward of 60° N.

The isotropic viscosity poleward of 20° is five times smaller in OM3.1 than OM3.0. To illustrate the impact in the coupled climate model, we ran the climate model CM2.1 for 100 years using an ocean component with the horizontal viscosity of OM3.0. Figure 16 shows a difference map of the 20 year mean barotropic quasi-streamfunction[15]. As might be expected, lowering the viscosity narrows and intensifies boundary currents. Somewhat unexpectedly, however, lowering the viscosity changes the structure of the interior gyres and overturning circulation.

The change in circulation is particularly clear in the Labrador Sea, where the Labrador gyre strengthens. Analysis of the vertical velocity shows that the lower viscosity run has much more downwelling at depth in this region, leading to a significant increase in vortex stretching in the upper water column. Associated with the increased

[15] As discussed in Sect. 17.2 of Griffies et al. (2004), there is no barotropic streamfunction in a free surface model since the vertically integrated transport has a nonzero divergence. However, for long time averages, the barotropic quasi-streamfunction $\psi^{(U)}(x,y) = -\int_{y_o}^{y} U(x,y')$ serves as a close approximation, where U is the vertically integrated zonal velocity.

Labrador Sea gyre is an increase in the overturning circulation (Fig. 17). Although the overturning increased signficantly, the northward heat transport only increased by a modest 0.1 PW upon reducing the viscosity.

Increases in circulation upon lowering viscosity are also found in the weakly stratified Southern Ocean, where the ACC spins up slightly from 126.5 to 132.1 Sv. Significant changes are found in currents through other key passages as well (Table 1), with the transports in the Florida Strait and Bering Strait significantly improved by lowering viscosity. Transports in the tropics remain relatively unchanged, as viscosity in this region remains the same.

The changes in circulation are associated with improvements in the simulated hydrography. Figure 18 compares the spatial distribution of the RMS temperature and salinity errors over the top 1500m in the two runs. Clear improvements are seen in the North Atlantic, where the spinup of the Labrador Sea gyre is associated with a breakdown of a fresh, cold cap. Over the North Atlantic the RMS temperature error drops from 2.39°C to 2.17°C, and the RMS salinity error drops from 0.73 to 0.69. Since the North Atlantic is the region where the RMS errors are largest, the decision was made to use the lower viscosities for CM2.1, even though doing so increases errors in other metrics, such as temperature in the North Pacific. Note that improvements in temperature error are much smaller than the changes associated with changing the winds from the different atmospheric models used in CM2.0 and CM2.1.

We close this section by noting that when attempting to lower the ocean viscosity in CM2.0, the solution worsened, particularly in the North Atlantic. Decreasing horizontal viscosity tends to move the boundary between the subpolar and subtropical gyres to the south. Since CM2.0 has wind stresses that were already shifted equatorward, decreasing the viscosity leads to an enhancement of an already strong bias. In CM2.1, a more realistic wind distribution enables us to use lower viscosities, which enabled us to improve other aspects of the circulation. This situation illustrates one of the difficulties in tuning coupled models, where choices made to tune one coupled model may not apply to a different coupled model with different biases and sensitivities.

3.5. Exchange with marginal seas

As noted in Sect. 2.2, the B-grid used in MOM4.0 requires two tracer points in order to connect ocean basins via a velocity point. This situation is problematic when marginal seas connect to the ocean through narrow passageways which are unresolved by the model grid. Such spuriously land-locked seas must be considered in the climate model in order to (1) conserve global budgets of water and tracer in the coupled climate system, and (2) allow the hydrography of the larger ocean basins to be affected by properties of the marginal seas. The Mediterranean salt tongue in the Atlantic is a canonical example where marginal sea properties strongly affect the water mass properties of a larger adjacent ocean basin.

There are two general options for handling critical unresolved passages: (1) modify the model's topography to open the passageway, thus allowing resolved transport between the marginal sea and ocean; (2) keep the marginal sea land-locked, but provide some indirect communication route. Depending on grid resolution and properties in the marginal sea, opening an unresolved passage may be quite reasonable. In other cases, it can result in far too much exchange between the two water bodies. The Strait of Gibraltar provides an example, where Spain is only about 12 km from Morrocco, thus requiring a very refined grid to explictly resolve this passage. Some coarse resolution global models, especially those based on the C-grid arrangement of model fields, successfully allow for an explicit advective flow connection between the Atlantic and Mediterranean without serious affects on the Atlantic water masses.

We chose to keep Gibraltar, and certain other passageways, closed to advective and diffusive transport in OM3, but to allow tracer exchange between the inland seas and the adjacent ocean basins through an exchange parameterization. In addition, volume exchange is available, and this is needed since moisture budgets in the climate system are generally not closed over individual basins. For example, there is a net evaporation over the Mediterranean and Red Seas. Without allowing volume to be exchanged with the Atlantic and Indian Oceans, respectively, the simulation would eventually dry up the

marginal sea grid cells.

Details of the exchange parameterization, known as "crossland mixing", are provided in the MOM4.0 documentation of Griffies et al. (2004). We expose here a few salient points since they have not been documented in the peer-reviewed literature. For this purpose, we make reference to the schematic in Fig. 19. Consider two grid cells at the same discrete vertical point, with one inside the marginal sea and the other outside. We prescribe an exchange of tracer and volume between these two cells via

$$\partial_t(h^{(1)}\,T^{(1)}) = \gamma^{(1)}\,(h^{(2)}\,T^{(2)} - h^{(1)}\,T^{(1)}) \tag{11}$$

$$\partial_t(h^{(2)}\,T^{(2)}) = \gamma^{(2)}\,(h^{(1)}\,T^{(1)} - h^{(2)}\,T^{(2)}) \tag{12}$$

$$\partial_t\,h^{(1)} = \gamma^{(1)}\,(h^{(2)} - h^{(1)}) \tag{13}$$

$$\partial_t\,h^{(2)} = \gamma^{(2)}\,(h^{(1)} - h^{(2)}). \tag{14}$$

In these equations, h is the tracer cell thickness, T is its tracer concentration, and γ is an exchange rate whose form is prescribed below. Note that the thickness has a nonzero tendency only for the top cell arising from undulations of the surface height. Furthermore, we do not allow exchange between cells adjacent to the bottom, since in this case their time independent thicknesses could be distinct due to partial step topography, in which case equations (13) and (14) become inconsistent.

The exchange coefficients which prescribe the strength of the mixing are given by

$$\gamma^{(1)} = \frac{2\,U}{A^{(1)}\,(H^{(1)}+H^{(2)})} \tag{15}$$

$$\gamma^{(2)} = \frac{2\,U}{A^{(2)}\,(H^{(1)}+H^{(2)})} \tag{16}$$

where A is the horizontal area of the tracer cell, H is its thickness under a resting ocean, and U is a prescribed volume per time exchange computed according to the caption to Fig. 19. The geometric factors ensure that the total tracer and volume are conserved by these processes.

There are a total of five unresolved marginal seas in OM3 which employ the crossland mixing scheme: (1) Mediterranean-Atlantic, (2) Black-Mediterranean, (3) Red-Indian, (4) Baltic-Atlantic, and (5) Hudson-Atlantic. All of the exchanges are prescribed

between more than a single point on each side of the passageway to reduce the possibility of initiating a spatial checkerboard mode commonly found on the B-grid (Killworth et al., 1991; Griffies et al., 2001)[16].

In addition to the crossland mixing described above, we found it essential to resolve the following difficulty associated with an ocean model whose volume can evolve. Consider the situation where the prescribed exchange rates for the crossland mixing scheme are suitable for reaching an equilibrium under stable climate forcing. That is, the volume of marginal sea water is at a steady state. Now allow for changes in climate forcing to alter the fresh water budget over the catchment basin for the marginal sea (e.g. increased evaporation over the Mediterranean). In this case, it is possible for the increased evaporation to outrun the volume exchanged with the ocean basin, and so to have the top grid cells in the marginal sea dry up.

To ensure that this scenario does not occur, we added yet another pathway for volume to be exchanged. Here, we exchange volume between the two regions at a rate directly proportional to the difference in surface heights between the basins. Hence, for example, if the Mediterranean starts to dry up faster than the exchange with the Atlantic facilitated via crossland mixing, then this additional pathway available via "crossland insertion" extracts more water from the Atlantic and inserts it into the Mediterranean. The insertion is over a column, with vertical adjustment processes leading to a stable column at the end of the process in a manner similar to the river discharge scheme discussed in Sect. 3.6.

The motivation for including the crossland transport parameterizations is clear, given the importance of marginal seas for the World Ocean. Nonetheless, it is interesting to see what affects they have on the coupled model simulation, and in particular what time

[16]This mode is damped in OM3.0 by the use of a Laplacian filter applied to the surface height. It is suppressed in OM3.1 by use of the predictor-corrector for the barotropic equations, which is a temporally dissipative time stepping scheme with smaller spatial scales preferentially dissipated (see Sect. 12.8.1.3 of Griffies, 2004). A biharmonic filter is also applied to the surface height in OM3.1.

scales are involved. For this purpose we configured CM2.1 in the standard way, yet removed both the crossland mixing and crossland insertion schemes. Within five years, the model came down because of excessive evaporation over the Red Sea causing the top model grid cell (10m thickness with a resting ocean) to dry[17]. In the region next to the Straits of Gibraltar on the Mediterranean side, the annual mean salinity averaged over 800–1200 m became quite salty (roughly 1.5 psu saltier) within the first year relative to the World Ocean Atlas of Conkright et al. (2002). Correspondingly, over the course of the five year experiment, the region extending westward from the Iberian Penisula in the Atlantic became progressively fresher (roughly 0.5 psu fresher) relative to Conkright et al. (2002). Both of these effects are expected in a model without transport of salty waters from the Mediterranean to the Atlantic.

3.6. River runoff into the ocean model

Both the CM2.0 and CM2.1 versions of the climate model have a land component with a river routing scheme, whereby precipitation and snow melt over land are routed into the ocean at selected points. Our experience has shown that inserting the river water into the surface grid cell of the ocean model causes numerical problems with too much fresh water stabilizing the water column through the lighter, less dense surface waters inhibiting mixing. This problem is enhanced with refined vertical grid spacing. In reality, river plumes tend to hug the coast and are stirred by breaking waves and tidal mixing. Such mixing processes are not resolved in our model.

To reduce the salinity errors that result without sufficient coastal mixing near river mouths, some climate models spread the river discharge over a wide region near the river mouths. Our approach is to introduce additional mixing at the river mouth where the river routing scheme prescribed the input of river water. To partially parameterize tidal mixing, we incorporated unresolved tidal velocity shears into the KPP boundary

[17]This problem would not have occurred in a rigid lid model. Instead, salinity in the Red Sea would increase without bound without any mixing with the fresher Indian Ocean.

layer scheme as discussed in Sect. 2.9. In addition, we inserted the river runoff over the upper four model grid cells (roughly 40m). In this approach, water is injected into vertical box labeled by the integer k, thus affecting tracer concentration within the box and causing an advective flux to the adjacent box $k-1$ above box k. If the modified temperature and salinity profile produces an unstable density profile, convection occurs to stabilize the two boxes. Fresh water is then inserted into box $k-1$ and the process continues.

Figure 20 compares the surface salinity in two CM2.1 experiments, one run with the standard 40 m insertion of river runoff and the other with only 10 m insertion. As in Fig. 10, we focus on the Arctic Ocean as its SSS is very sensitive to the treatment of rivers. As expected, the SSS is generally fresher in the case with only 10 m insertion than the standard CM2.1 experiment, with regions near river mouths noticeably fresher.

4. Concluding remarks

The purpose of this paper was to describe the physical and numerical algorithms used to construct the ocean component to the GFDL coupled climate model CM2. Two model versions were considered, with differences in the ocean component arising from alternative time stepping schemes and modifications to the lateral subgrid scale parameterizations. In general, we endeavoured to rationalize the many choices and compromises required to build a global ocean climate model. This discussion included the often omitted "ad hoc" steps that can be unsatisfying scientifically, but are frequently made to facilitate practical and timely advances.

There are shortcomings to what we have developed. How some of the problems affect the climate simulation are discussed in Gnanadesikan et al. (2005). Others are associated with any "ad hoc" and unsatisfying approaches documented here, such as the representations of overflows, exchange with marginal seas, and the need to tune subgrid parameters without a first principles basis. Producing models that are more fully justified from first principles, either physically or numerically, is a nontrival goal

that will hopefully arise with further research and development[18].

Nonetheless, this document details the most realistic ocean climate model produced by GFDL. It is arguably amongst the state-of-the-art in the world today. Novel features include the following:

- Nonlinear explicit free surface with real fresh water forcing rather than virtual tracer fluxes,
- A newly implemented time stepping scheme that ensures local and global tracer conservation, avoids the computational mode present with the leap frog scheme, and is twice as stable as the leap frog for our climate model configuation thus allowing for halving the ocean model computational cost,
- State-of-the-art treatment of parameterized neutral physics fluxes as they interact with the surface mixed layer, and use of a novel flow dependent diffusivity to determine the strength of the fluxes.

This model has been used for century scale climate research of the coupled ocean and sea ice system, as the ocean component in the GFDL coupled climate model versions CM2.0 and CM2.1, and as the physical component of ocean biogeochemical/ecosystem models which are presently being developed for more complete earth system model purposes. Research with this model has also been conducted for seasonal-interannual forecasting and predictability, and multi-decadal global ocean analyses have been produced using a data assimilation system. Some of these applications are represented in the papers by Gnanadesikan et al. (2005), Delworth et al. (2005), Wittenberg et al. (2005), and Stouffer et al. (2005).

[18]To facilitate the evolution of OM3 beyond that form documented here, both the ocean and sea ice components are supported by GFDL for use by the international community though the distribution of the Modular Ocean Model version 4 (MOM4.0). The code has been successfully ported to many computational platforms, and it comes with support tools and test cases of use for various modelling activities.

The merger of diverse research and application streams represents a major advance in the collaborative use of intellectual and computational resources at GFDL, where in the past, many of these streams were represented by a broader array of models whose utility for complementary research was limited. It is likely that future advances in global ocean and climate modelling will likewise require focused efforts of numerous scientists and engineers, each providing valuable and essential contributions using a wide array of expertise, experience, and insight.

The construction of the latest GFDL coupled climate model has occupied the bulk of GFDL's intellectual and computational resources since 1999. Many other labs have recently completed similar exercises with analogous resource allocation. This time has seen tremendous improvements in computational power, software frameworks, and numerical and physical understanding of what it takes to create a coupled climate model. Many areas of modelling will certainly improve during the next round of model development. Full disclosure of the model fundamentals, facilitated by peer-reviewed papers such as this one, is essential to provide a firm stepping stone towards the next model generation.

Appendix A: MOM4.0 equations and methods

The purpose of this appendix is to summarize the model equations and numerical methods forming the basis for the MOM4.0 code. Algorithms are based on the Boussinesq and hydrostatic approximations using surfaces of geopotential, or z-coordinates, to discretize the vertical, and generalized orthogonal horizontal coordinates to tile the sphere. The methods for spatial and temporal discretization of the primitive equations are based on their thickness weighted form. Some of the material here complements the temporal discretization discussed in Sect. 3.2.

The main reference for the following material is the book by Griffies (2004) and the technical manual by Griffies et al. (2004), as well as other references given below.

A.1: Momentum equation

The balance of thickness weighted horizontal Boussinesq momentum $\rho_o\, h\,(u,v)=\rho_o\, h\,\mathbf{u}$ for a grid level k is written[19].

$$[\,\partial_t+(\mathcal{M}+f)\,\hat{\mathbf{z}}\times\,]\,(h\,\mathbf{u}) = -\nabla\cdot(h\,\mathbf{u}\,\mathbf{u})-(h/\rho_o)\,\nabla\,p+h\,\mathbf{F}+[\,w\,\mathbf{u}-\kappa\,\mathbf{u}_{,z}\,]_k-[\,w\,\mathbf{u}-\kappa\,\mathbf{u}_{,z}\,]_{k-1}. \quad (17)$$

As commonly formulated for B-grid ocean models, this equation is written in advective form, which contrasts to the vector invariant form (see Sect. 4.4.4 of Griffies, 2004) typically used to formulate C-grid ocean models (Griffies et al., 2000a). The field h is the thickness (in meters) of the model's discrete velocity cell. It is a function of space and time for the top model grid cell whose thickness changes according to undulations of the free upper surface, yet it is static for deeper cells. We now further describe terms appearing in this equation and mention the discrete numerical methods used to compute them.

– The Boussinesq reference density has the value

$$\rho_o = 1035\,\mathrm{kg\,m^{-3}}. \quad (18)$$

This value is convenient since the ocean density generally varies less than 2% from it (see page 47 of Gill, 1982), whereas the more traditional (e.g. Cox, 1984) reference density of $1000\,\mathrm{kg\,m^{-3}}$ is less accurate.

– The advective metric frequency (Eq. 4.49 of Griffies, 2004)

$$\mathcal{M} = v\,\partial_x \ln \mathrm{d}y - u\,\partial_y \ln \mathrm{d}x \quad (19)$$

arises from the advection of momentum on the curved space of the sphere. It takes on the familiar form $(u/R)\tan\phi$ for spherical coordinates, where the horizontal grid distances are $(\mathrm{d}x,\mathrm{d}y)=R\,(\cos\phi\,\mathrm{d}\lambda,\mathrm{d}\phi)$, with R the earth's radius, ϕ

[19] Discrete vertical labels k are exposed only where needed.

the latitude, and λ the longitude. However, in generalized orthogonal coordinates as used in MOM4.0, $\mathcal{M}$ is specified only when coordinate distances dx and dy are set by the choice of horizontal coordinates.

– Except near the equator, the advective metric frequency $\mathcal{M}$ is much smaller than the Coriolis parameter

$$f = 2\,\Omega\,\sin\phi, \tag{20}$$

with $\Omega = 7.292 \times 10^{-5}\ \mathrm{s}^{-1}$ the earth's rotation rate. The Coriolis force $-f\,\hat{\mathbf{z}} \times \mathbf{u}$ is naturally discretized on the B-grid, since the horizontal velocity components (u, v) are both placed at the same point. Temporal discretization of the Coriolis force can be written

$$-f\,\hat{\mathbf{z}} \times \mathbf{u} \longrightarrow -f\,\hat{\mathbf{z}} \times [\,\mathbf{u}(\tau)\,(1-\alpha) + \mathbf{u}(\tau+1)\,\alpha\,], \tag{21}$$

with τ the model's baroclinic time step. Setting α=0 recovers the explicit Coriolis force, α=1 is implicit, and α=1/2 is semi-implicit. The semi-implicit approach ensures second order accuracy (e.g. Bryan, 1989; Durran, 1999) and is used in CM2. Notably, the effects on velocity from the Coriolis force can be solved analytically with a B-grid placement of the horizontal velocity components. However, this analytic approach is not commonly done in ocean climate modelling because of the utility of implicit or semi-implicit time stepping methods to damp inertial-like instabilities, such as those arising from the coupled ocean sea ice system.

– The thickness weighted advection of momentum

$$\text{advection} = -\nabla\cdot(h\,\mathbf{u}\,\mathbf{u}) + (w\,\mathbf{u})_k - (w\,\mathbf{u})_{k-1} \tag{22}$$

is discretized in space using the traditional second order centred differences, with origins in the methods of Bryan (1969a) and Cox (1984). Such facilitates a convenient transfer of energy within the discrete model in a manner analogous to the continuum (Bryan, 1969a; Semtner, 1974).

At the ocean surface, the vertical transport of horizontal momentum arises from the transport of water across the ocean free surface via

$$(w\,\mathbf{u})_{k=0} = -q_{\mathrm{w}}\,\mathbf{u}_{\mathrm{w}}, \tag{23}$$

where we choose a water velocity equal to that in the adjacent top model grid cell

$$\mathbf{u}_{\mathrm{w}} = \mathbf{u}_{k=1}. \tag{24}$$

The transport q_{w} measures the volume per time of water crossing the ocean free surface per unit horizontal area (equation (3.41) of Griffies, 2004)

$$q_{\mathrm{w}}\,\mathrm{d}A = \hat{\mathbf{n}}\cdot\hat{\mathbf{n}}_{w}\,(P - E + R + I)\,\mathrm{d}A_{\hat{\mathbf{n}}}, \tag{25}$$

where $\mathrm{d}A_{\hat{\mathbf{n}}}$ is the area element on the free ocean surface, $\mathrm{d}A=\mathrm{d}z\,\mathrm{d}y$ is the horizontal area element on the sphere, $\hat{\mathbf{n}}$ is the outward normal at the free surface, and $\hat{\mathbf{n}}_{w}$ orients the water transport. Additionally, $P>0$ for precipitation, $E>0$ for evaporation, $R>0$ for river runoff into the ocean, and $I>0$ for sea ice melting, each of which have dimensions of a velocity, or volume per time per area.

– The horizontal friction vector $\mathbf{F}$ dissipates kinetic energy, and it arises from horizontal strains in the simulated ocean fluid. In Sect. 3.4 we illustrate sensitivity of the simulation to two settings for this friction. The mathematical formulation and numerical discretization of this operator are detailed in Part 5 of Griffies (2004). Notably, there is no fundamental theory for friction in ocean climate models, so it is generally tuned to yield simulations with desirable properties.

– The term $-\rho_o\,\kappa\,\mathbf{u}_{,z}$ in principle represents the vertical downgradient flux of horizontal momentum due to unresolved SGS processes.[20] It dissipates kinetic energy when there are vertical shears in the fluid. The precise value of the viscosity

[20]The comma notation for partial derivative, $\partial_z\,\mathbf{u}=\mathbf{u}_{,z}$, is a shorthand used in this appendix.

κ is not well known, and so its value in our simulations is determined via tuning. In CM2, κ is specified according to a constant background of $10^{-4}\,\mathrm{m}^2\,\mathrm{s}^{-1}$ in addition to the KPP scheme discussed in Sect. 2.9.

– As noted in Sect. 2.5, the hydrostatic pressure p is diagnosed from in situ density, with density diagnosed from the equation of state using knowledge of the potential temperature, salinity, as well as the previous time step's pressure (Eq. 1). The pressure is located on the tracer grid, which is coincident with density. Hence, the horizontal pressure gradient ∇p must be averaged onto the B-grid velocity location, which lies at the tracer corners. We choose second order difference and averaging operations.

  A spatial average in one direction of a finite difference taken in the orthogonal direction leads to computational null modes. Such modes are unphysical and so should be suppressed, as done via the use of nontrivial levels of friction (Killworth et al., 1991; Griffies et al., 2001). In contrast, the use of very small or zero levels of friction readily expose these modes, which appear as a checkerboard or zig-zag pattern in the velocity between alternating grid cells.

  Because of the partial bottom steps used to represent topography (Fig. 4), the bottom grid cells generally have different thicknesses. Hence, there are two terms needed to compute horizontal pressure gradients in the bottom most grid cells. The first arises from the difference in pressure between the adjacent cells, and the second arises from slopes in the bottom topography. This calculation is analogous to that needed for ocean models using topography-following vertical coordinates. Importantly, however, this calculation is needed here only for the bottom-most grid cell in a particular column. Pacanowski and Gnanadesikan (1998) further detail this importanat technical point.

A.2: Tracer equation

The thickness weighted tracer equation at a discrete depth level k takes the following form in continuous time and continuous horizontal space

$$\partial_t (hT) = -\nabla \cdot [h(\mathbf{u}T + \mathbf{F})] + h\mathcal{S}^{(T)} \qquad + (wT + F^z)_k - (wT + F^z)_{k-1}. \tag{26}$$

For material tracers such as salinity and nutrients, the dimensionless tracer concentration T represents the mass of tracer per mass of seawater within a parcel of fluid. Its evolution is described by the above scalar conservation law whereby its value is determined by the convergence of thickness weighted advective fluxes

$$\text{advection} = -\nabla \cdot (h\mathbf{u}T) \qquad + (wT + F^z)_k - (wT + F^z)_{k-1}, \tag{27}$$

the convergence of SGS fluxes $(\mathbf{F}, F^z)$, and sources $\mathcal{S}^{(T)}$. Evolution of the thermodynamical tracer potential temperature θ is also described by this equation (see Sect. 5 of Griffies, 2004, for fundamentals of the tracer equation).

Discretization of advective fluxes are discussed in Sect. 2.6. Sections 2.8 and 2.9 describe parameterizations that specify the diapycnal tracer flux implemented as downgradient vertical diffusion

$$F^z = -\kappa T_{,z} \tag{28}$$

where κ is a diapycnal tracer diffusivity. Finally, Sect. 3.3 outlines our approach for including SGS neutral physics processes in the simulations. We implement neutral physics according to the methods described by Griffies et al. (1998) and Griffies (1998), where the tracer flux arising from SGS neutral physics is given by

$$F^m = -J^{mn} T_{,n} \tag{29}$$

where the summation convention is followed. The second order SGS tracer transport tensor J^{mn} is given by

$$\mathbf{J} = \begin{pmatrix} A_l & 0 & (A_l - A_{gm}) \\ 0 & A_l & (A_l - A_{gm}) \\ (A_l + A_{gm}) & (A_l + A_{gm}) & S^2 A_l \end{pmatrix}, \tag{30}$$

where A_l is the neutral diffusivity and A_{gm} is the skew-diffusivity associated with the scheme of Gent and McWilliams (1990) and Gent et al. (1995). S is the magnitude of the neutral slope $\mathbf{S}$, which is computed via

$$\mathbf{S} = -\left(\frac{\rho_{,\theta}\nabla\theta + \rho_{,s}\nabla s}{\rho_{,\theta}\theta_{,z} + \rho_{,s}s_{,z}}\right), \tag{31}$$

where $\rho_{,\theta}$ and $\rho_{,s}$ are the partial derivatives of density with respect to potential temperature and salinity, respectively. The SGS transport tensor in equation (30) results from combining the small slope neutral diffusion tensor with the skew diffusion tensor representing the Gent and McWilliams (1990) and Gent et al. (1995) eddy induced transport. Use of the combined transport tensor is not dependent on taking the same values for the diffusivities A_l and A_{gm}, although this choice does result in the very simple horizontal downgradient form for the two horizontal flux components.

A.3: Vertically integrated budgets

To exploit the factor of 50–100 between the speeds of fast barotropic waves and slow baroclinic waves and advection, MOM4.0 approximates the fast modes by time stepping the vertically integrated volume and momentum budgets with a small time step, whereas the slower three-dimensional dynamics are updated using longer time steps. This method and its benefits are discussed in Sect. 3.1. Here, we simply expose the equations.

The budget for volume within a column of Boussinesq seawater leads to the evolution equation for the ocean surface height η

$$\eta_{,t} = -\nabla \cdot \mathbf{U} + q_{\mathrm{w}} + \mathcal{S}^{(\eta)}. \tag{32}$$

Here,

$$\mathbf{U} = \int_{-H}^{\eta} \mathrm{d}z\, \mathbf{u} \tag{33}$$

is the horizontal velocity integrated from the ocean bottom at $z=-H$ to the free surface at $z=\eta$, q_{w} is the water transport across the free surface (equation (25)), and $\mathcal{S}^{(\eta)}$ is a volumn source in the column. Correspondingly, a vertical sum of the thickness weighted momentum Eq. (17) leads to the two-dimensional system

$$\rho_o\,(\partial_t + f\,\hat{\mathbf{z}}\times)\,\mathbf{U} = -(H+\eta)\;\nabla p_{\mathrm{s}} + \rho_o\,\mathbf{G}. \tag{34}$$

Here, $p_{\mathrm{s}}=\rho\, g\, \eta$ is the pressure at $z=0$ associated with mass in the region between $z = 0$ and $z=\eta$, and $\mathbf{G}$ is the vertical sum of the remaining terms appearing in Eq. (17).

Acknowledgements. This work is the result of a large number of people at GFDL over recent years. We thank in particular those in computer systems and modelling services who provided technical assistance in keeping the model running on the many different computational platforms employed during development. B. Hallberg remained throughout this development a generous source of fruitful suggestions and honest guidance. A. Adcroft and R. Stouffer provided very useful critical comments on various drafts of this paper. And we thank J. Mahlman and A. Leetmaa, the two directors of GFDL during the course of this project, for their sincere support and encouragement.

References

Adcroft, A. and Campin, J.-M.: Rescaled height coordinates for accurate representation of free-surface flows in ocean circulation models, Ocean Modelling, 7, 269–284, 2004. 174

Adcroft, A., Hill, C., and Marshall, J.: Representation of topography by shaved cells in a height coordinate ocean model, Monthly Weather Review, 125, 2293–2315, 1997. 175

Anderson, J. L., Balaji, V., Broccoli, A. J., Cooke, W. F., Delworth, T. L., Dixon, K. W., Donnor, L. J., Dunne, K. A., Freidenreich, S. M., Garner, S. T., Gudgel, R. G., Gordon, C., Held, I. M., Hemler, R. S., Horowitz, L. W., Klein, S. A., Knuttson, T. R., Kushner, P. J., Langenhorst, A. R., Lau, N.-C., Liang, Z., Malyshev, S. L., Milly, P., Nath, M. J., Ploshay, J. J., Ramaswany, V., Schwarzkopf, M. D., Shevliakova, E., Sirutis, J. J., Soden, B. J., Stern, W. F., Thompson, L. A., Wilson, R. J., Wittenberg, A. T., and Wyman, B. L.: The GFDL Global Atmospheric Model Development Team: The new GFDL global atmosphere and land model AM2/LM2: Evaluation with prescribed SST simulations, Journal of Climate, 17, 4641–4673, 2005. 169

Beckers, J. M., Burchard, H., Campin, J.-M., Deleersnijder, E., and Mathieu, P. P.: Another reason why simple discretizations of rotated diffusion operators cause problems in ocean models: Comments on isoneutral diffusion in a z-coordinate ocean model, Journal of Physical Oceanography, 28, 1552–1559, 1998. 198

Beckers, J. M., Burchard, H., Deleersnijder, E., and Mathieu, P. P.: Numerical discretization of rotated diffusion operators in ocean models, Monthly Weather Review, 128, 2711–2733, 2000. 198

Beckmann, A.: The representation of bottom boundary layer processes in numerical ocean circulation models, in Ocean Modeling and Parameterization, edited by E. P. Chassignet and J. Verron, vol. 516 of NATO ASI Mathematical and Physical Sciences Series, Kluwer, 135–154, 1998. 176

Beckmann, A. and Döscher, R.: A method for improved representation of dense water spreading over topography in geopotential-coordinate models, Journal of Physical Oceanography, 27, 581–591, 1997. 177

Bryan, F.: Parameter sensitivity of primitive equation ocean general circulation models, Journal of Physical Oceanography, 17, 970–985, 1987. 181

Bryan, K.: A numerical method for the study of the circulation of the world ocean, Journal of Computational Physics, 4, 347–376, 1969a. 168, 184, 210

Bryan, K.: Climate and the ocean circulation III: The ocean model, Monthly Weather Review, 97, 806–824, 1969b. 168

Bryan, K.: The design of numerical models of the ocean circulation, in: Oceanic Circulation Models: Combining Data and Dynamics, edited by: Anderson, D. L. and Willebrand, J., vol. 284 of NATO ASI Series. Series C, Kluwer Academic Publishers, 465–511, 1989. 210

Bryan, K. and Cox, M. D.: A numerical investigation of the oceanic general circulation, Tellus, XIX, 54–80, 1967. 168

Bryan, K. and Cox, M. D.: An approximate equation of state for numerical models of the ocean circulation, Journal of Physical Oceanography, 4, 510–514, 1972. 178

Bryan, K. and Lewis, L. J.: A water mass model of the world ocean, Journal of Geophysical Research, 84, 2503–2517, 1979. 181, 182, 233

Bryan, K., Manabe, S., and Pacanowski, R. C.: A global ocean-atmosphere climate model. Part II. The oceanic circulation, Journal of Physical Oceanography, 5, 30–46, 1975. 171

Bryan, K., Dukowicz, J. K., and Smith, R. D.: On the Mixing Coefficient in the Parameterization of Bolus Velocity, Journal of Physical Oceanography, 29, 2442–2456, 1999. 197

Campin, J.-M., Adcroft, A., Hill, C., and Marshall, J.: Conservation of properties in a free-surface model, Ocean Modelling, 6, 221–244, 2004. 188, 193

Conkright, M., Antonov, J., Baranova, O., Boyer, T., Garcia, H., Gelfeld, F., Johnson, D., Locarnini, R., Murphy, P., O'Brien, T., Smolyar, I., and Stephens, C.: World Ocean Database 2001, Volume 1: Introduction, NOAA Atlas NESD'is 42, U.S. Government Printing Office 13, NOAA, Washington, D.C., 167 pp., 2002. 205, 226, 239, 244

Cox, M. D.: A Primitive Equation, 3-Dimensional Model of the Ocean, NOAA/Geophysical Fluid Dynamics Laboratory, Princeton, USA, 1984. 209, 210

Cunningham, S., Alderson, S., King, B., and Brandon, M.: Transport and variability of the Antarctic Circumpolar Current in Drake Passage, Journal of Geophysical Research, 108, Art. 8084, 2003. 226

Danabasoglu, G., McWilliams, J. C., and Gent, P.: The role of mesoscale tracer transports in the global ocean circulation, Science, 8, 1123–1126, 1994. 194

Delworth, T. L., Broccoli, A. J., Rosati, A., Stouffer, R. J., Balaji, V., Beesley, J. A., Cooke, W. F., Dixon, K. W., Dunne, J., Dunne, K. A., Durachta, J. W., Findell, K. L., Ginoux, P., Gnanadesikan, A., Gordon, C., Griffies, S. M., Gudgel, R., Harrison, M. J., Held, I. M., Hemler, R. S., Horowitz, L. W., Klein, S. A., Knutson, T. R., Kushner, P. J., Langenhorst, A. L., Lee, H.-C., Lin, S., Lu, L., Malyshev, S. L., Milly, P., Ramaswamy, V., Russell, J., Schwarzkopf, M. D., Shevliakova, E., Sirutis, J., Spelman, M., Stern, W. F., Winton, M., Wittenberg, A. T., Wyman, B., Zeng, F., and Zhang, R.: GFDL's CM2 Global Coupled Climate Models – Part 1: Formulation and Simulation Characteristics, Journal of Climate, submitted, 2005. 166, 169, 182, 183, 207, 238

Dewar, W. K., Hsueh, Y., McDougall, T. J., and Yuan, D.: Calculation of Pressure in Ocean

Simulations, Journal of Physical Oceanography, 28, 577–588, 1998. 178
Doney, S. C. and Hecht, M. W.: Antarctic Bottom Water formation and deep water chlorofluorocarbon distributions in a global ocean climate model, Journal of Physical Oceanography, 32, 1642–1666, 2002. 177
Döscher, R. and Beckmann, A.: Effects of a bottom boundary layer parameterization in a coarse-resolution model of the North Atlantic Ocean, Journal of Atmospheric and Oceanic Technology, 17, 698–707, 1999. 177
Durran, D. R.: Numerical Methods for Wave Equations in Geophysical Fluid Dynamics, Springer Verlag, Berlin, 470 pp, 1999. 188, 189, 192, 193, 210
Egbert, G., Bennett, A., and Foreman, M.: TOPEX/POSEIDON tides estimated using inverse model, Journal of Geophysical Research, 99, 24 821–24 852, 1994. 235
Feistel, R. and Hagen, E.: On the Gibbs thermodynamic potential of seawater, Progress in Oceanography, 36, 249–327, 1995. 178
Gent, P. R. and McWilliams, J. C.: Isopycnal mixing in ocean circulation models., Journal of Physical Oceanography, 20, 150–155, 1990. 194, 196, 197, 214, 239
Gent, P. R., Willebrand, J., McDougall, T. J., and McWilliams, J. C.: Parameterizing eddy-induced tracer transports in ocean circulation models, Journal of Physical Oceanography, 25, 463–474, 1995. 194, 214, 243
Gerdes, R., Köberle, C., and Willebrand, J.: The influence of numerical advection schemes on the results of ocean general circulation models, Climate Dynamics, 5, 211–226, 1991. 198
Gill, A.: Atmosphere-Ocean Dynamics, vol. 30 of International Geophysics Series, Academic Press, London, 662 + xv pp, 1982. 178, 209
Gnanadesikan, A.: A simple predictive model for the structure of the oceanic pycnocline, Science, 283, 2077–2079, 1999a. 194
Gnanadesikan, A.: A global model of silicon cycling: Sensitivity to eddy parameterization and dissolution, Global Biogeochemical Cycles, 13, 199–220, 1999b. 195
Gnanadesikan, A.: Numerical issues for coupling biological models with isopycnal mixing schemes, Ocean Modelling, 1, 1–15, 1999c. 195
Gnanadesikan, A., Slater, R., Gruber, N., and Sarmiento, J.: Oceanic vertical exchange and new production: A comparison between models and data, Deep Sea Research II, 49, 363–401, 2002. 195
Gnanadesikan, A., Slater, R., and Samuels, B.: Sensitivity of water mass transformation and heat transport to subgridscale parameterization in ocean general circulation models, Geo-

physical Research Letters, 30, 1967, doi: 10.1029/2003GL018 036, 2003. 181, 195
Gnanadesikan, A., Dixon, K. W., Griffies, S. M., Balaji, V., Beesley, J. A., Cooke, W. F., Delworth, T. L., Gerdes, R., Harrison, M. J., Held, I. M., Hurlin, W. J., Lee, H.-C., Liang, Z., Nong, G., Pacanowski, R. C., Rosati, A., Russell, J., Samuels, B. L., Song, S. M., , Spelman, M. J., Stouffer, R. J., Sweeney, C. O., Vecchi, G., Winton, M., Wittenberg, A. T., Zeng, F., and Zhang, R.: GFDL's CM2 Global Coupled Climate Models-Part 2: The Baseline Ocean Simulation, Journal of Climate, submitted, 2005. 166, 169, 206, 207
Gordon, A., Susanto, R., and Vranes, K.: Cool Indonesian throughflow as a consequence of restricted surface layer flow, Nature, 425, 824–828, 2003. 226
Greatbatch, R. J. and Li, G.: Alongslope mean flow and an associated upslope bolus flux of tracer in a parameterization of mesoscale turbulence, Deep-Sea Research, 47, 709–735, 2000. 196
Gregg, M., Sanford, T., and Winkel, D.: Reduced mixing from the breaking of internal waves in equatorial waters, Nature, 422, 513–515, 2003. 181
Griffies, S. M.: The Gent-McWilliams skew-flux, Journal of Physical Oceanography, 28, 831–841, 1998. 194, 198, 213
Griffies, S. M.: Fundamentals of ocean climate models, Princeton University Press, Princeton, USA, 496 pages, 2004. 185, 188, 192, 196, 197, 199, 204, 208, 209, 211, 213
Griffies, S. M. and Hallberg, R. W.: Biharmonic friction with a Smagorinsky viscosity for use in large-scale eddy-permitting ocean models, Monthly Weather Review, 128, 2935–2946, 2000. 199, 200
Griffies, S. M., Gnanadesikan, A., Pacanowski, R. C., Larichev, V., Dukowicz, J. K., and Smith, R. D.: Isoneutral diffusion in a z-coordinate ocean model, Journal of Physical Oceanography, 28, 805–830, 1998. 181, 194, 198, 213
Griffies, S. M., Böning, C., Bryan, F. O., Chassignet, E. P., Gerdes, R., Hasumi, H., Hirst, A., Treguier, A.-M., and Webb, D.: Developments in Ocean Climate Modelling, Ocean Modelling, 2, 123–192, 2000a. 168, 174, 176, 188, 193, 209
Griffies, S. M., Pacanowski, R. C., and Hallberg, R. W.: Spurious diapycnal mixing associated with advection in a z-coordinate ocean model, Monthly Weather Review, 128, 538–564, 2000b. 194, 199
Griffies, S. M., Pacanowski, R., Schmidt, R., and Balaji, V.: Tracer Conservation with an Explicit Free Surface Method for z-coordinate Ocean Models, Monthly Weather Review, 129, 1081–1098, 2001. 174, 178, 184, 185, 188, 192, 204, 212

Griffies, S. M., Harrison, M. J., Pacanowski, R. C., and Rosati, A.: A Technical Guide to MOM4, NOAA/Geophysical Fluid Dynamics Laboratory, Princeton, USA, 337 pp, 2004. 200, 203, 208, 227

Hallberg, R. and Gnanadesikan, A.: An exploration of the role of transient eddies in determining the transport of a zonally reentrant current, Journal of Physical Oceanography, 31, 3312–3330, 2001. 197

Hallberg, R. W.: Stable split time stepping schemes for large-scale ocean modeling, Journal of Computational Physics, 135, 54–65, 1997. 173, 188, 193

Haltiner, G. T. and Williams, R. T.: Numerical Prediction and Dynamic Meteorology, John Wiley and Sons, New York, USA, 1980. 188, 192

Held, I. M. and Larichev, V. D.: A scaling theory for horizontally homogeneous baroclinically unstable flow on a beta plane, Journal of Atmospheric Sciences, 53, 946–952, 1996. 197

Held, I. M. and Schneider, T.: The surface branch of the zonally averaged mass transport circulation in the troposphere, Journal of Atmospheric Sciences, 56, 1688–1697, 1999. 195

Holland, W. R., Chow, J. C., and Bryan, F. O.: Application of a third-order upwind scheme in the NCAR ocean model, Journal of Climate, 11, 1487–1493, 1998. 179, 190

Huang, R. X.: Real freshwater flux as a natural boundary condition for the salinity balance and thermohaline circulation forced by evaporation and precipitation, Journal of Physical Oceanography, 23, 2428–2446, 1993. 184

Hundsdorfer, W. and Trompert, R.: Method of lines and direct discretization: a comparison for linear advection, Applied Numerical Mathematics, pp. 469–490, 1994. 179

Jakobssen, M., Chervis, N., Woodward, J., Macnab, R., and Coakley, B.: New grid of Arctic bathymetry aids scientists and mapmakers, EOS Transactions of the American Geophysical Union, 81, 89, 93, 96, 2000. 175

Kantha, L. H. and Clayson, C. A.: Small Scale Processes in Geophysical Fluid Flows, Academic Press, New York, USA, 883 pp, 2000. 183

Karoly, D., McIntosh, P., Berrisford, P., McDougall, T. J., and Hirst, A.: Similarities of the Deacon cell in the Southern Ocean and Ferrel cells in the atmosphere, Quarterly Journal of the Royal Meteorological Society, 123, 519–526, 1997. 197

Killworth, P. D., Stainforth, D., Webb, D. J., and Paterson, S. M.: The development of a free-surface Bryan-Cox-Semtner ocean mode, Journal of Physical Oceanography, 21, 1333–1348, 1991. 192, 204, 212

Large, W. G., McWilliams, J. C., and Doney, S. C.: Oceanic vertical mixing: A review and a

model with a nonlocal boundary layer parameterization, Reviews of Geophysics, 32, 363–403, 1994. 183, 235

Large, W. G., Danabasoglu, G., Doney, S. C., and McWilliams, J. C.: Sensitivity to surface forcing and boundary layer mixing in a global ocean model: annual-mean climatology, Journal of Physical Oceanography, 27, 2418–2447, 1997. 195

Large, W. G., Danabasoglu, G., McWilliams, J. C., Gent, P. R., and Bryan, F. O.: Equatorial circulation of a global ocean climate model with anisotropic horizontal viscosity, Journal of Physical Oceanography, 31, 518–536, 2001. 183, 199, 200

Latif, M., Anderson, D., Barnett, T., Cane, M., Kleeman, R., Leetmaa, A., O'Brien, J., Rosati, A., and Schneider, E.: A review of the predictability and prediction of ENSO, Journal of Geophysical Research, 103, 14 375–14 393, 1998. 173

Leaman, K., Molinari, R., and Vertes, P.: Structure and variability of the Florida Current at 27N: April 1982-July 1984, Journal of Physical Oceanography, 17, 565–583, 1987. 226

Ledwell, J. R., Watson, A. J., and Law, C. S.: Evidence for slow mixing across the pycnocline from an open-ocean tracer-release experiment, Nature, 364, 701–703, 1993. 181

Lee, H.-C., Rosati, A., and Spelman, M.: Barotropic tidal mixing effects in a coupled climate model: Oceanic conditions in the northern Atlantic, Ocean Modelling, accepted, 2005. 183, 235

Leonard, B. P.: A stable and accurate convective modelling procedure based on quadratic upstream interpolation, Computer Methods in Applied Mechanics and Engineering, 19, 59–98, 1979. 179

Lin, S.-J.: A vertically lagrangian finite-volume dynamical core for global models, Monthly Weather Review, 2293–2307, 2004. 169

Madec, G. and Imbard, M.: A global ocean mesh to overcome the North Pole singularity, CD, 12, 381–388, 1996. 172

Maier-Reimer, E., Hasselmann, K., Olbers, D., and Willebrand, J.: An ocean circulation model for climate studies, Max-Plank-Institut für Meteorologie, Hamburg, Germany, 34 pp, 1983. 181

Manabe, S. and Bryan, K.: Climate calculations with a combined ocean-atmosphere model, Journal of Atmospheric Sciences, 26, 786–789, 1969. 168

Marshall, J., Olbers, D., Ross, H., and Wolf-Gladrow, D.: Potential vorticity constraints on the dynamics and hydrography of the Southern Ocean, Journal of Physical Oceanography, 23, 465–487, 1993. 197

Marshall, J., Hill, C., Perelman, L., and Adcroft, A.: Hydrostatic, quasi-hydrostatic, and nonhydrostatic ocean modeling, Journal of Geophysical Research, 102, 5733–5752, 1997. 188, 193

McDougall, T. J.: Neutral surfaces, Journal of Physical Oceanography, 17, 1950–1967, 1987. 194

McDougall, T. J. and Church, J. A.: Pitfalls with numerical representations of isopycnal and diapycnal mixing, Journal of Physical Oceanography, 16, 196–199, 1986. 194

McDougall, T. J. and McIntosh, P. C.: The temporal-residual-mean velocity. Part II: isopycnal interpretation and the tracer and momentum equations., Journal of Physical Oceanography, 31, 1222–1246, 2001. 195

McDougall, T. J., Jackett, D. R., Wright, D. G., and Feistel, R.: Accurate and computationally efficient algorithms for potential temperature and density of seawater., Journal of Atmospheric and Oceanic Technology, 20, 730–741, 2003. 178

Meehl, G., Gent, P. R., Arblaster, J., Otto-Bliesner, B., Brady, E., and Craig, A.: Factors that affect the amplitude of El Niño in global coupled climate models, Climate Dynamics, 17, 515–526, 2001. 182

Morel, A. and Antoine, D.: Heating rate within the upper ccean in relation to its bio-optical state, Journal of Physical Oceanography, 24, 1652–1665, 1994. 180

Murray, R. J.: Explicit generation of orthogonal grids for ocean models, Journal of Computational Physics, 126, 251–273, 1996. 172, 227

Murtugudde, R., Beauchamp, J., McClain, C. R., Lewis, M., and Busalacchi, A. J.: Effects of penetrative radiation on the upper tropical ocean circulation, Journal of Climate, 2002. 174

NOAA: Data Announcement 88-MGG-02, Digital relief of the Surface of the Earth, Tech. rep., NOAA, National Geophysical Data Center, Boulder, Colorado, 1988. 175

Ohlmann, J.: Ocean Radiant Heating in Climate Models, JOC, 16, 1337–1351, 2003. 180

Olbers, D. J., Wenzel, M., and Willebrand, J.: The inference of North Atlantic circulation patterns from climatological hydrographic data, Reviews of Geophysics, 23, 313–356, 1985. 194

Pacanowski, R. C.: Effect of equatorial currents on surface stress, Journal of Physical Oceanography, 17, 833–838, 1987. 191

Pacanowski, R. C. and Gnanadesikan, A.: Transient response in a z-level ocean model that resolves topography with partial-cells, Monthly Weather Review, 126, 3248–3270, 1998. 175, 212

Pacanowski, R. C. and Griffies, S. M.: The MOM3 Manual, NOAA/Geophysical Fluid Dynamics

Laboratory, Princeton, USA, 680 pp, 1999. 171, 179, 190
Park, Y.-G. and Bryan, K.: Comparison of thermally driven circulations from a depth-coordinate model and an isopycnal-layer model. Part I: scaling-law sensitivity to vertical diffusivity, Journal of Physical Oceanography, 30, 590–605, 2000. 181
Polzin, K. L., Speer, K., Toole, J. M., and Schmitt, R. W.: Intense mixing of Antarctic bottom water in the equatorial Atlantic, Nature, 380, 54–57, 1996. 181
Polzin, K. L., Toole, J. M., Ledwell, J. R., and Schmitt, R. W.: Spatial variability of turbulent mixing in the abyssal ocean, Science, 276, 93–96, 1997. 181, 182
Rahmstorf, S.: A fast and complete convection scheme for ocean models, Ocean Modelling, 101, 9–11, 1993. 196
Redi, M. H.: Oceanic isopycnal mixing by coordinate rotation., Journal of Physical Oceanography, 12, 1154–1158, 1982. 194
Roach, A., Aagard, K., Pease, C., Salo, S., Weingartner, T., Pavlov, V., and Kulakov, M.: Direct measurements of transport and water properties through Bering Strait, Journal of Geophysical Research, 100, 18 443–18 457, 1995. 226
Roberts, M. J. and Marshall, D.: Do we require adiabatic dissipation schemes in eddy-resolving ocean models?, Journal of Physical Oceanography, 28, 2050–2063, 1998. 194
Roberts, M. J. and Wood, R.: Topographic sensitivity studies with a Bryan-Cox-type ocean model, Journal of Physical Oceanography, 27, 823–836, 1997. 176
Schmitt, R. W.: Double diffusion in oceanography, Annual Review of Fluid Mechanics, 26, 255–285, 1994. 183
Schneider, E., DeWitt, D., Rosati, A., Kirtman, B., Link, J., and Tribbia, J.: Retrospective ENSO forecasts: sensitivity to atmospheric model and ocean resolution, Monthly Weather Review, 131, 3038–3060, 2003. 173
Semtner, A. J.: An oceanic general circulation model with bottom topography, in Numerical Simulation of Weather and Climate, Technical Report No. 9, UCLA Department of Meteorology, 1974. 210
Simmons, H. L., Jayne, S. R., Laurent, L. C. S., and Weaver, A. J.: Tidally driven mixing in a numerical model of the ocean general circulation, Ocean Modelling, 6, 245–263, 2004. 182
Smagorinsky, J.: General circulation experiments with the primitive equations: I. The basic experiment, Monthly Weather Review, 91, 99–164, 1963. 200
Smagorinsky, J.: Some historical remarks on the use of nonlinear viscosities, in Large Eddy Simulation of Complex Engineering and Geophysical Flows, edited by B. Galperin and S. A.

Orszag, pp. 3–36, Cambridge University Press, 1993. 200
Smith, K. S. and Vallis, G. K.: The scales and equilibration of midocean eddies: forced-dissipative flow, Journal of Physical Oceanography, 32, 1699–1721, 2002. 197
Smith, R. D. and McWilliams, J. C.: Anisotropic horizonal viscosity for ocean models, Ocean Modelling, 5, 129–156, 2003. 199
Smith, W. H. F. and Sandwell, D. T.: Global seafloor topography from satellite altimetry and ship depth soundings, Science, 277, 1957–1962, 1997. 175
Solomon, H.: On the representation of isentropic mixing in ocean models, Journal of Physical Oceanography, 1, 233–234, 1971. 194
Stacey, M. W., Pond, S., and Nowak, Z. P.: A Numerical Model of the Circulation in Knight Inlet, British Columbia, Canada, Journal of Physical Oceanography, 25, 1037–1062, 1995. 174
Stammer, D.: Global characteristics of ocean variability estimated from regional TOPEX/POSEIDON altimeter measurements, Journal of Physical Oceanography, 27, 1743–1769, 1997. 197
Stone, P.: A simplified radiative-dynamical model for the static stability of rotating atmospheres, Journal of Atmospheric Sciences, 29, 405–418, 1972. 197
Stouffer, R. J., Broccoli, A., Delworth, T., Dixon, K., Gudgel, R., Held, I., Hemler, R., Knutsn, T., Lee, H.-C., Schwarzkopf, M., Soden, B., Spelman, M., Winton, M., and Zeng, F.: GFDL's CM2 Global coupled climate models: Part 4: idealized climate response, Journal of Climate, submitted, 2005. 166, 169, 207
Sweby, P.: High-resolution schemes using flux limiters for hyperbolic conservation-laws, SIAM Journal of Numerical Analysis, 21, 995–1011, 1984. 179
Sweeney, C., Gnanadesikan, A., Griffies, S. M., Harrison, M., Rosati, A., and Samuels, B.: Impacts of shortwave penetration depth on large-scale ocean circulation and heat transport, Journal of Physical Oceanography, in press, 2005. 180, 232
Toole, J. M. and McDougall, T. J.: Mixing and stirring in the ocean interior, in Ocean Circulation and Climate: Observing and Modelling the Global Ocean, edited by G. Siedler, J. Gould, and J. Church, Academic Press, 337–356, 2001. 183
Toole, J. M., Polzin, K. L., and Schmitt, R. W.: Estimates of diapycnal mixing in the abyssal ocean, Science, 264, 1120–1123, 1994. 181
Toole, J. M., Schmitt, R. W., and Polzin, K. L.: Near-boundary mixing above the flanks of a mid-latitude seamount, Journal of Geophysical Research, 102, 947–959, 1997. 181
Treguier, A. M., Held, I. M., and Larichev, V. D.: On the parameterization of quasi-geostrophic

eddies in primitive equation ocean models, Journal of Physical Oceanography, 27, 567–580, 1997. 195, 196, 198

Visbeck, M., Marshall, J. C., Haine, T., and Spall, M.: Specification of eddy transfer coefficients in coarse resolution ocean circulation models, Journal of Physical Oceanography, 27, 381–402, 1997. 197

Wajsowicz, R. C.: Models of the Southeast Asian Seas, Journal of Physical Oceanography, 29, 986–1018, 1999. 176

Whitehead, J. and Worthington, L.: The flux and mixing rates of Antarctic Bottom Water within the North Atlantic, Journal of Geophysical Research, 87, 7903–7924, 1982. 181

Winton, M., Hallberg, R. W., and Gnanadesikan, A.: Simulation of density-driven frictional downslope flow in *z*-coordinate ocean models, Journal of Physical Oceanography, 28, 2163–2174, 1998. 176

Wittenberg, A., Rosati, A., Lau, G., and Ploshay, J.: Tropical simulations with the recent GFDL coupled climate model, Journal of Climate, submitted, 2005. 166, 169, 200, 207

Table 1. Vertically integrated transports and root-mean-square (RMS) errors for CM2.1 simulations using the standard low viscosity and a higher value as used in CM2.0. Statistics are based on 20 year means. The observed Drake Passage transport is taken from Cunningham et al. (2003). Indonesian throughflow is from Gordon et al. (2003), Florida Current from Leaman et al. (1987), and Bering Strait from Roach et al. (1995). The RMS errors for potential temperature and salinity are relative to Conkright et al. (2002).

Transport or Field	observations	high viscosity	low viscosity
Florida Straits (Sv)	28.7-34.7	17.0	26.9
Drake Passage (Sv)	134	126.5	132.1
Bering Strait (Sv)	0.83	0.57	0.81
Indonesian Throughflow (Sv)	$\tilde{1}0$	14.2	14.1
Global temperature (C) RMSE	0.0	1.22	1.17
Global salinity (psu) RMSE	0.0	0.32	0.30
North Atlantic temperature (C) RMSE	0.0	2.39	2.17
North Atlantic salinity (psu) RMSE	0.0	0.73	0.69
North Pacific temperature (C) RMSE	0.0	1.34	1.38
North Pacific salinity (psu) RMSE	0.0	0.21	0.20

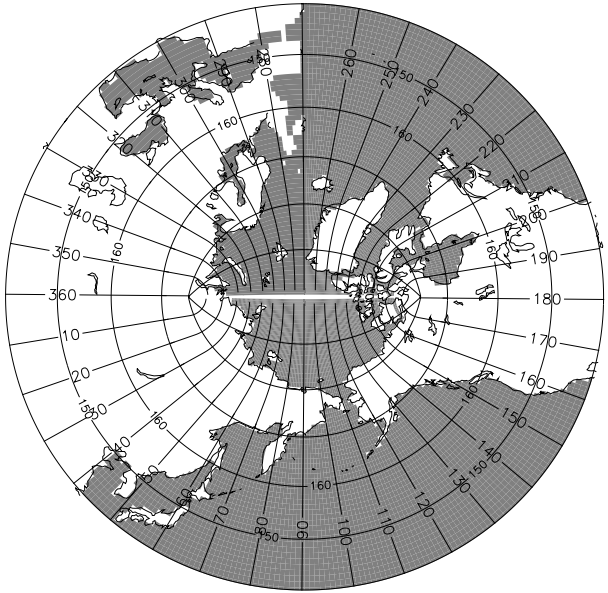

Fig. 1. Illustration of the bipolar Arctic as prescribed by Murray (1996) (see his Fig. 7) and realized in OM3. The transition from the bipolar Arctic to the spherical grid occurs at 65° N. We denote horizontal grid cells by (i, j) indices. As in the spherical coordinate region of the grid, lines of constant i–index move in a generalized eastward direction within the bipolar region. They start from the bipolar south pole at $i = 0$, which is identified with $i = ni$, where ni is the number of points along a latitude circle and $ni = 360$ in OM3. The bipolar north pole is at $i = ni/2$, which necessitates that ni be an even number. Both poles are centered at a velocity point on the B-grid used in MOM4.0. Lines of constant j move in a generalized northward direction. The bipolar prime-meridian is situated along the j-line with $j = nj$, where $nj = 200$ in OM3. This line defines the bipolar fold that bisects the tracer grid. Care must be exercised when mapping fields across this fold. As noted by Griffies et al. (2004), maintaining the exact identity of fields computed redundantly along the fold is essential for model stability. Note that the cut across the bipolar fold is a limitation of the graphics package, and does not represent a land-sea boundary in the model domain.

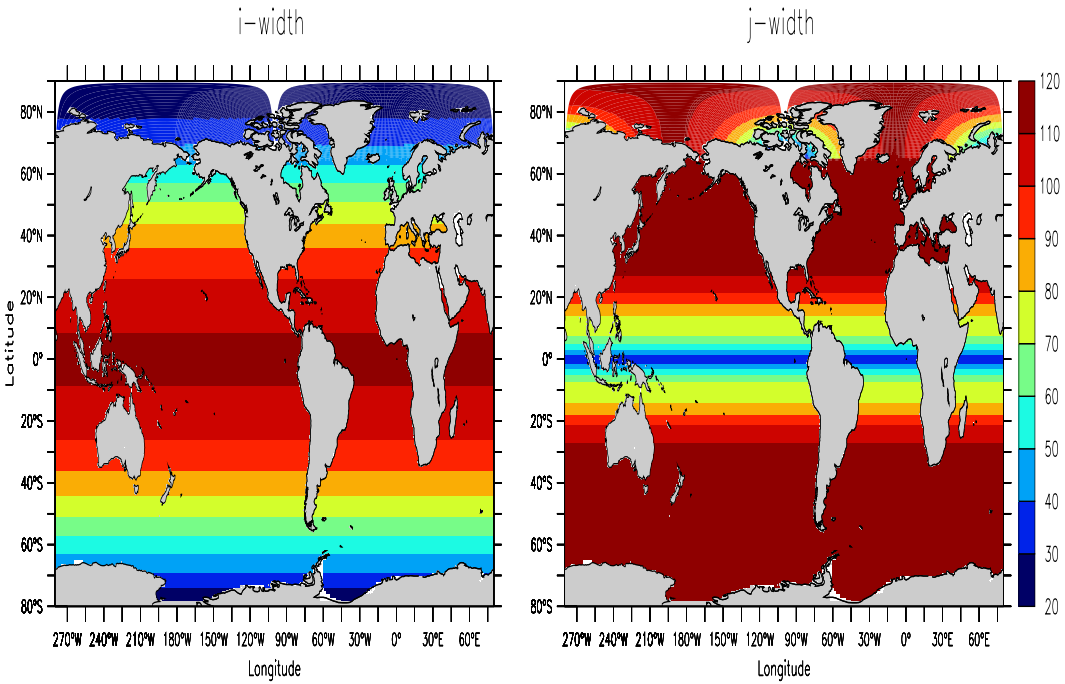

Fig. 2. Horizontal resolution of OM3 in units of kilometers. Left panel: generalized zonal (i) distance. The decrease in grid cell width moving towards the high southern latitudes is given by the cosine of the latitude. Right panel: generalized meridional (j) distance. Northward of 30° S, the meridional spacing is refined to 1/3° at the equator. It then coarsens again to 1° at 30° N, and stays there until reaching the bipolar region at 65° N. There are a total of 360 zonal grid points and 200 grid points over the latitude range 78° S to 90° N.

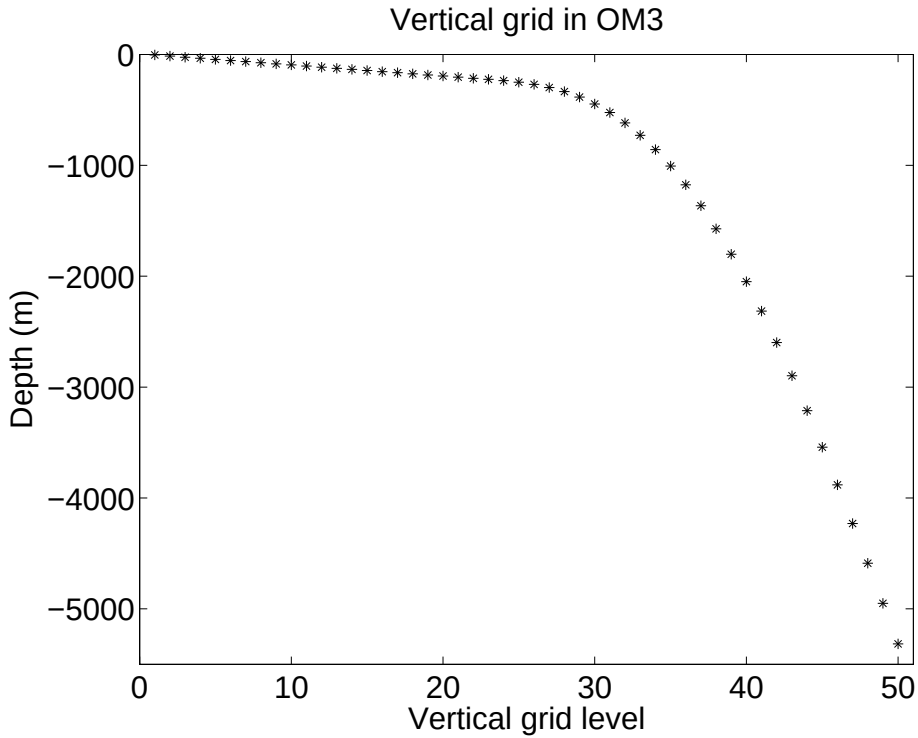

Fig. 3. Centers of the grid cells in the vertical for OM3. There are a total of 50 grid cells, with 22 evenly spaced in the upper 220 m. The deepest ocean grid point is at 5500 m. Deeper regions in the real ocean are relatively few and thought to be of minor consequence for climate.

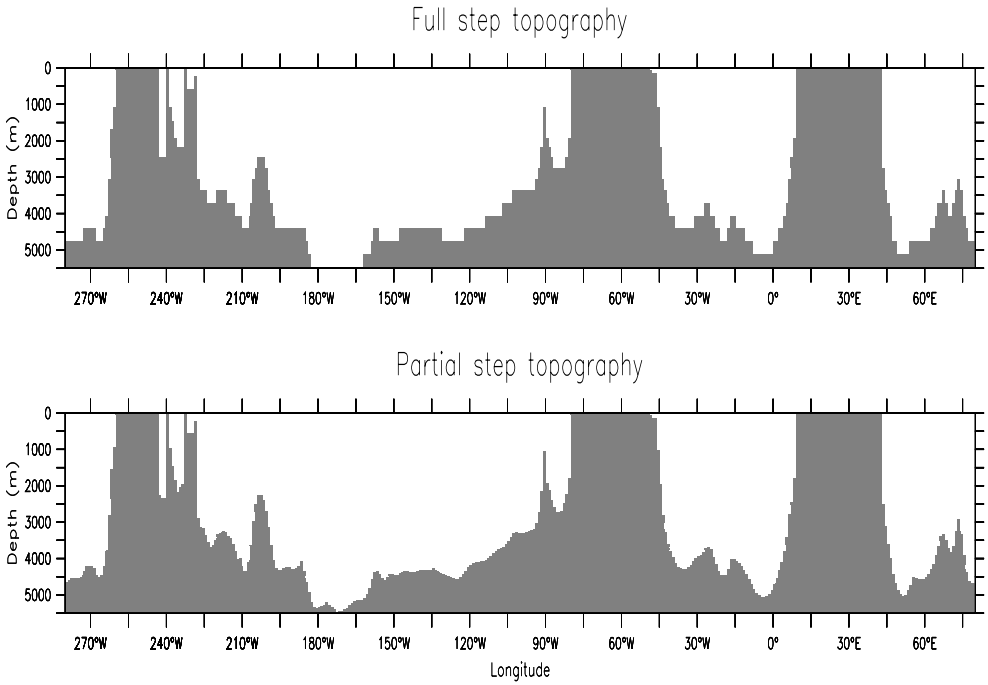

Fig. 4. Bottom topography along the equator for the tracer cells. This figure illustrates the difference between the older full step representation of the bottom topography (upper) and the partial step representation used in OM3 (lower). Note the large differences especially in regions where the topographic slope is modest and small.

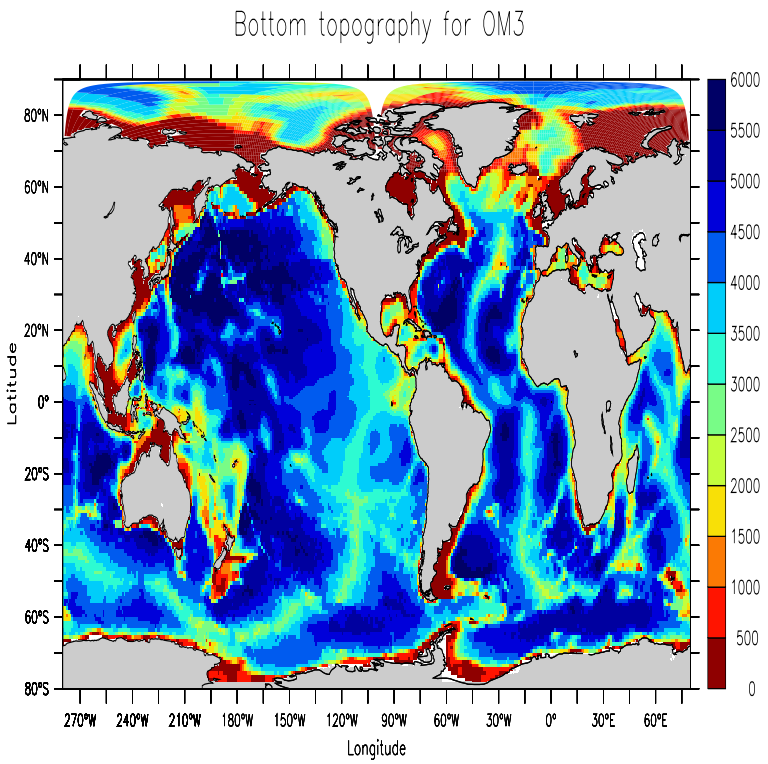

Fig. 5. The bottom depth for the tracer cells used in OM3. This topography and related html documentation can be downloaded from http://nomads.gfdl.noaa.gov.

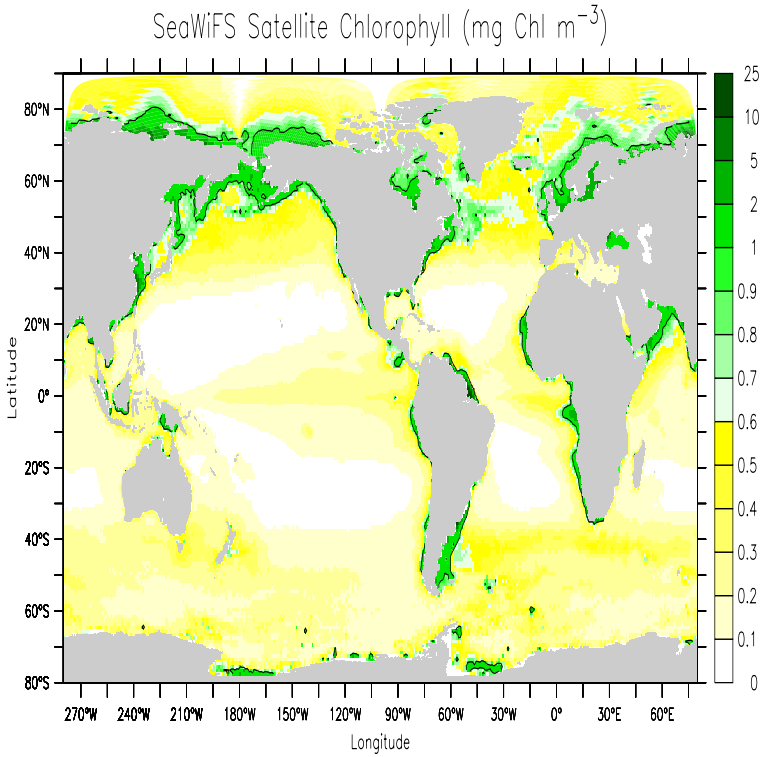

Fig. 6. Log10 of the annual mean chlorophyll concentration (mg/m^3) taken from the climatology developed by Sweeney et al. (2005). Note the larger values near coasts and in the polar regions are associated with high levels of biological activity in the colder and nutrient rich waters. Also, the equator is seen in both the Atlantic and Pacific as a result of increased biology in equatorial upwelling zones.

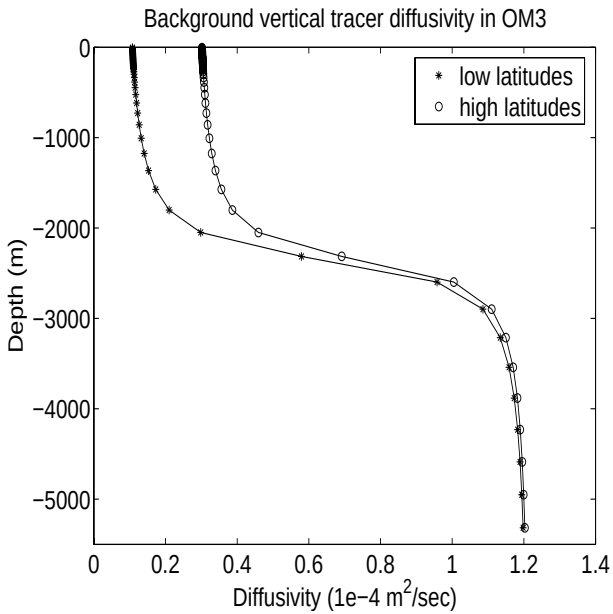

Fig. 7. Background vertical tracer diffusivity used in OM3 as suggested by Bryan and Lewis (1979). The surface values in the tropics are $0.1 \times 10^{-4}\,\mathrm{m}^2\,\mathrm{s}^{-1}$, whereas they are increased in the high latitudes to $0.3 \times 10^{-}4\,\mathrm{m}^2\,\mathrm{s}^{-1}$.

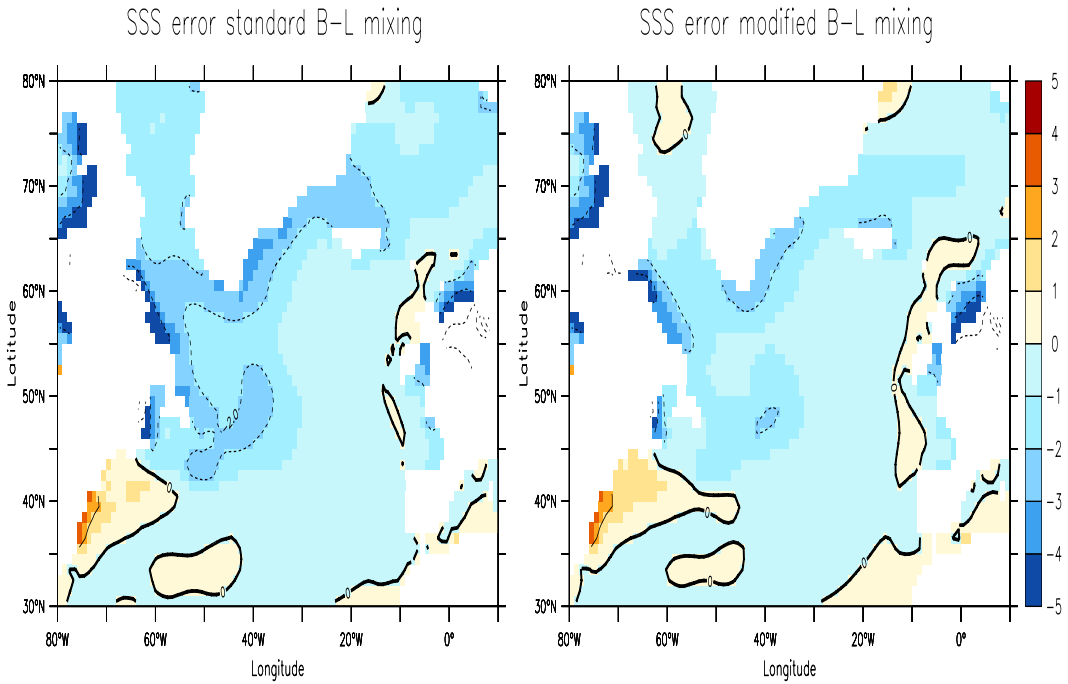

Fig. 8. Biases in the surface salinity for two runs of the CM2.0 coupled model where the Bryan-Lewis background vertical diffusivity in the high latitudes is altered according to Fig. 7. The model was run for 60 years, with biases determined over years 41–60. Left panel: bias for the standard run with Bryan-Lewis tracer diffusivity the same globally. Right panel: bias using the larger upper ocean Bryan-Lewis diffusivity in the higher latitudes. Note the reduced bias in the Labrador Sea and Greenland Sea deepwater formation regions.

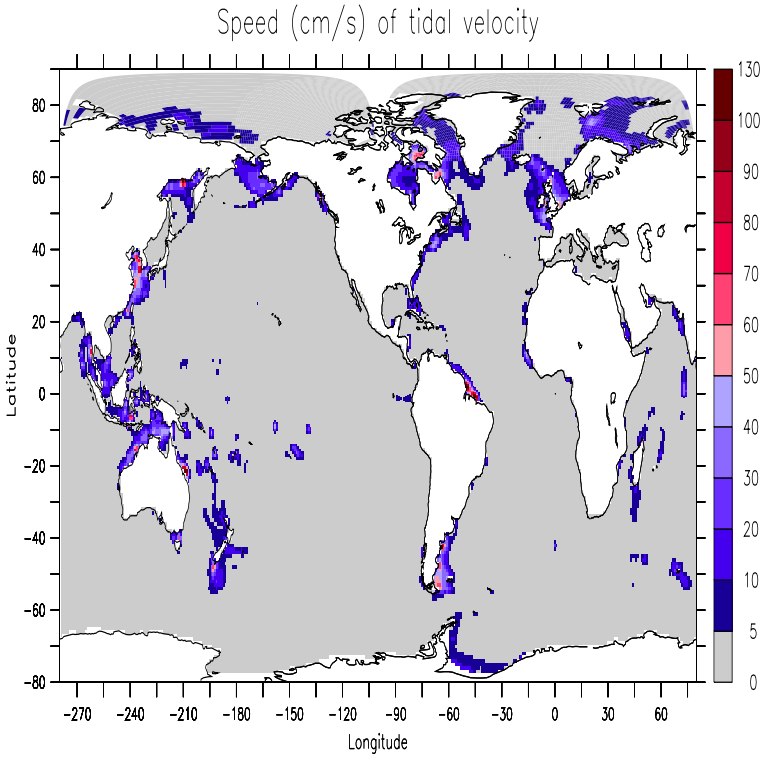

Fig. 9. Horizontal distribution of the maximum speed of the M2 tidal component from satellite data according to (Egbert et al., 1994). This speed is used to enhance the vertical shear in the computation of the Richardson number in the Large et al. (1994) boundary layer scheme in a manner described by Lee et al. (2005). Regions where the speed is high, such as near the coasts, result in enhanced mixing.

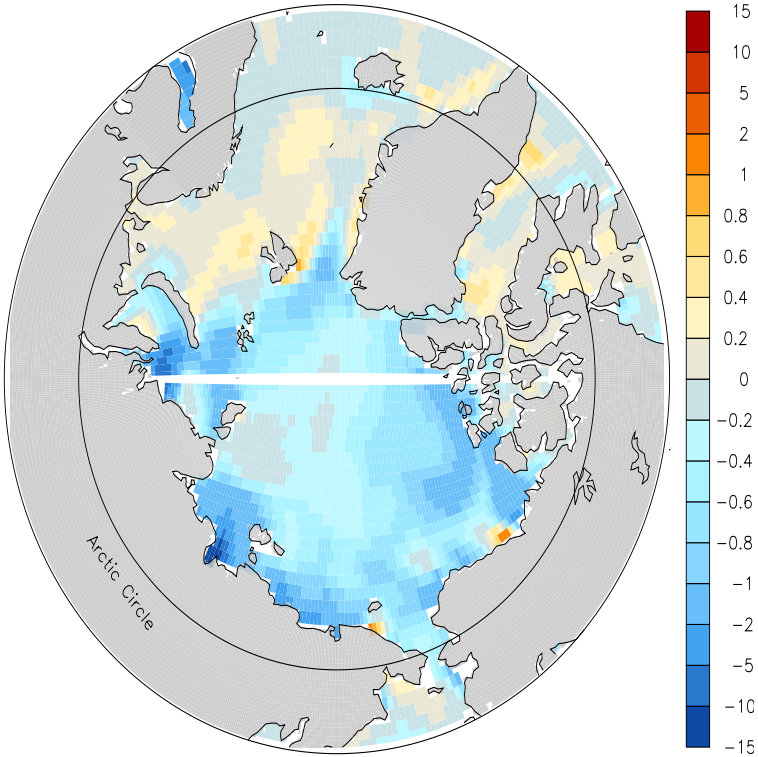

Fig. 10. Difference in Arctic surface salinity during August of the second year of integration in two CM2.1-like experiments. One experiment uses real water fluxes as in CM2.1, and the other uses virtual salt fluxes. The virtual salt flux experiment shows significantly fresher waters near river mouths, with local differences reaching 14 psu.

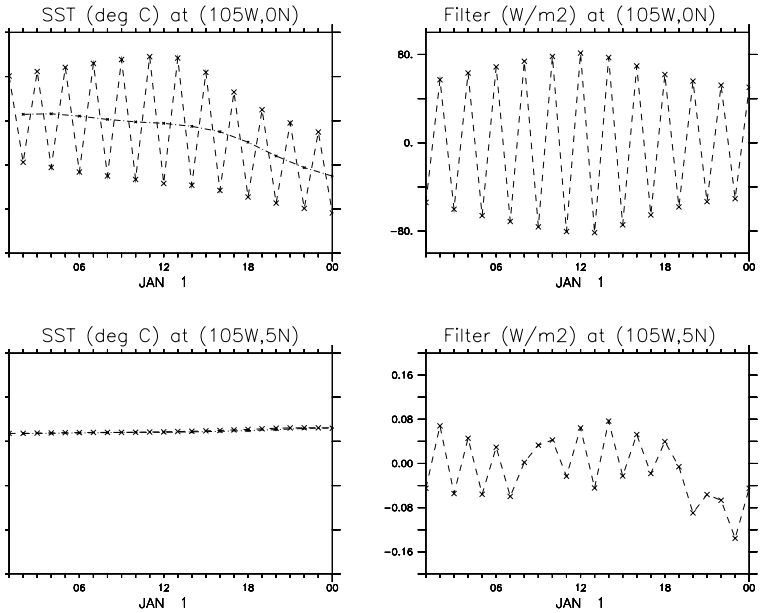

Fig. 11. Upper left panel: Instantaneous sea surface temperature over 1 January at (105° W, 0° N) as realized in a simulation using the leap frog scheme with an hour tracer time step (noisy time series) and the staggered scheme with a 2 h tracer time step (smooth time series). Upper right panel: Surface heating applied at (105° W, 0° N) from the Robert-Asselin time filter used to damp the leap frog splitting mode. Lower left panel: Instantaneous sea surface temperature over a single day at (105° W, 5° N) as realized in a simulation using the leap frog scheme with an hour tracer time step and the staggered scheme with a 2 h tracer time step. Note the width of the temperature range is set the same as at the equator. In general, the agreement of the solution off the equator, where the leapfrog splitting is minimal, is far greater than on the equator. Lower right panel: Surface heating applied at (105° W, 5° N) from the Robert-Asselin filter. Note the much smaller magnitude relative to the values on the equator.

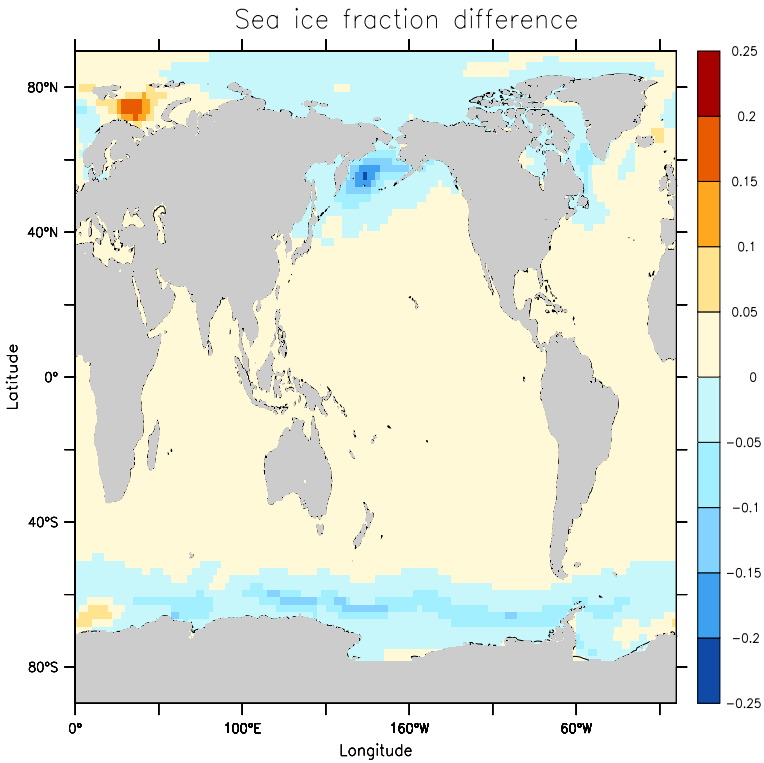

Fig. 12. Difference in sea ice fraction found in CM2.1 for the standard simulation with a constant neutral diffusivity of $A_l = 600\text{m}^2\,\text{s}^{-1}$ from a simulation where $A_l = A_{gm}$ as determined according to flow properties (as in CM2.0). The reduction in ice extent in the North Pacific found in the constant neutral diffusivity case reduced (though did not remove) biases in the coupled model towards too much ice in this region (see Fig. 14 of Delworth et al., 2005). Increases in ice extent in the high latitudes of the North Atlantic, however, increased model biases. Nonetheless, changes found with the constant neutral diffusivity outweighed the negatives, thus prompting the decision to use this setting in CM2.1.

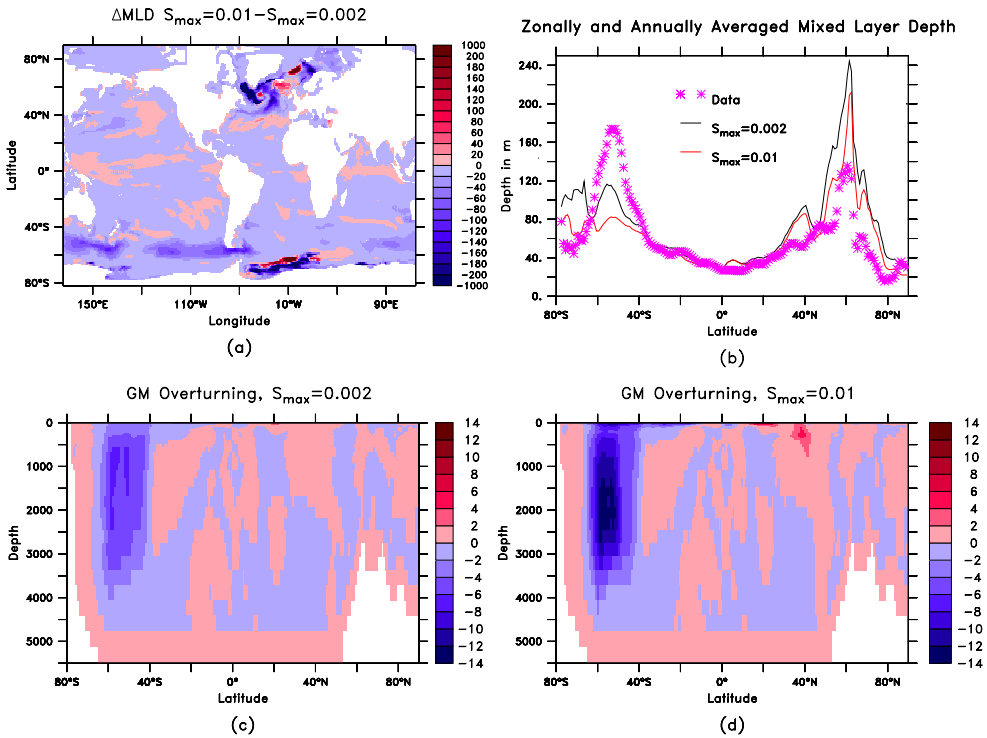

Fig. 13. Effects of changing the maximum slope above which the neutral physics schemes are exponentially tapered. Results shown here are years 6–10 of a spinup using CM2.1, so they may contain transient changes although we believe the general trend to be robust. **(a)** Change in mixed layer depth. **(b)** Zonally averaged mixed layer depth compared with Conkright et al. (2002). **(c)** Overturning associated with the zonally integrated quasi-Stokes transport from Gent and McWilliams (1990) in units of Sv with S_{max} = 0.002 as in CM2.0 and CM2.1. **(d)** Overturning from the quasi-Stokes transport with S_{max} = 0.01. Note the much larger transport, especially in the Southern Ocean, with this larger value of S_{max}.

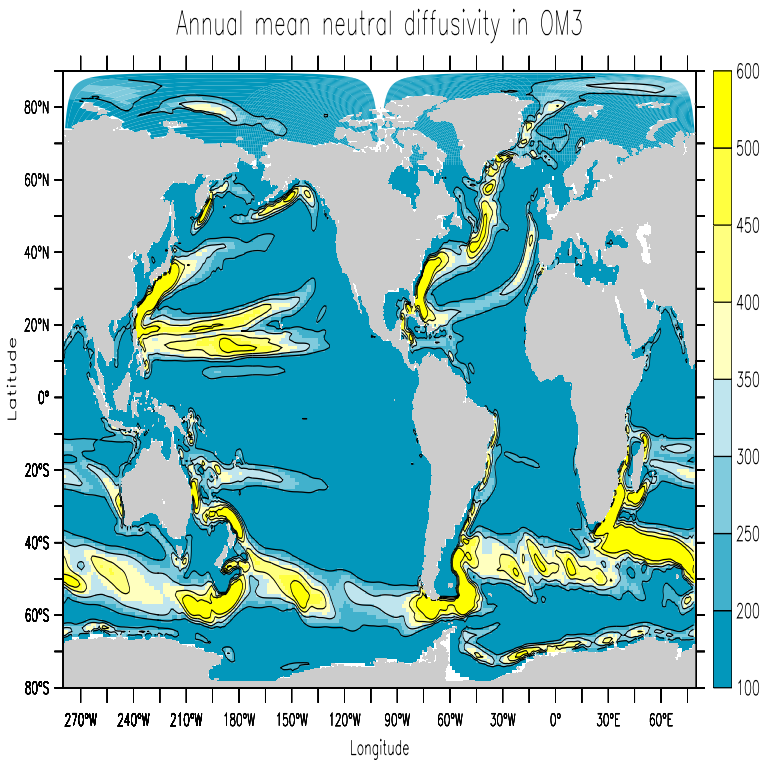

Fig. 14. Time mean diffusivity from CM2.1 over years 96–100. The minimum diffusivity is set to 100 $m^2 s^{-1}$ and maximum is 600 $m^2 s^{-1}$. This diffusivity is used just for the skew diffusivity in OM3.1. However, a similar prognostic diffusivity is used for both the neutral diffusivity and skew diffusivity in OM3.0.

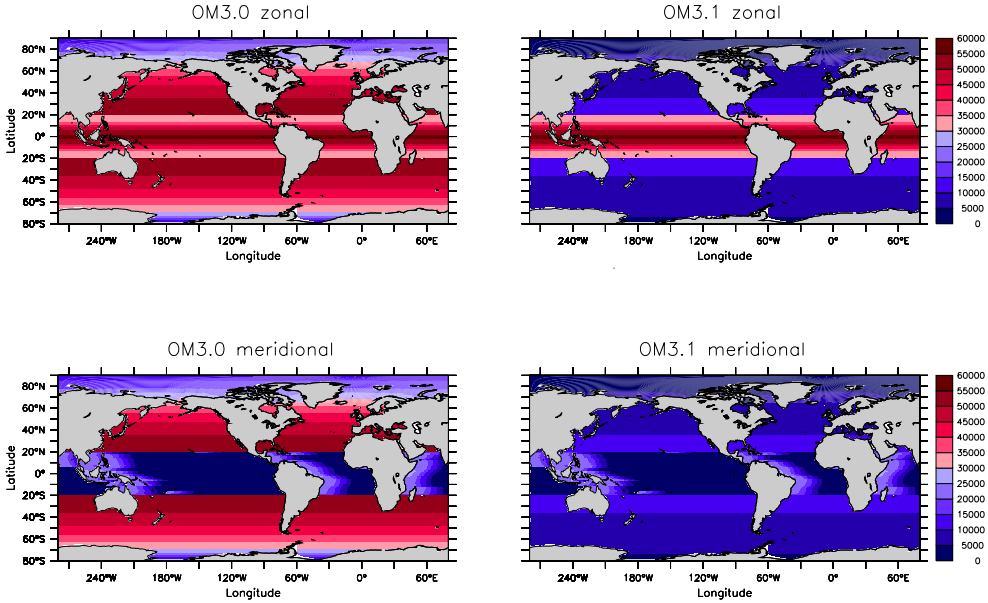

Fig. 15. Time independent zonal (upper) and meridional (lower) viscosities ($m^2 s^{-1}$) used in OM3.0 and OM3.1 at the ocean surface. Note the values are the same in the tropics, but they are five times smaller in OM3.1 poleward of 20°.

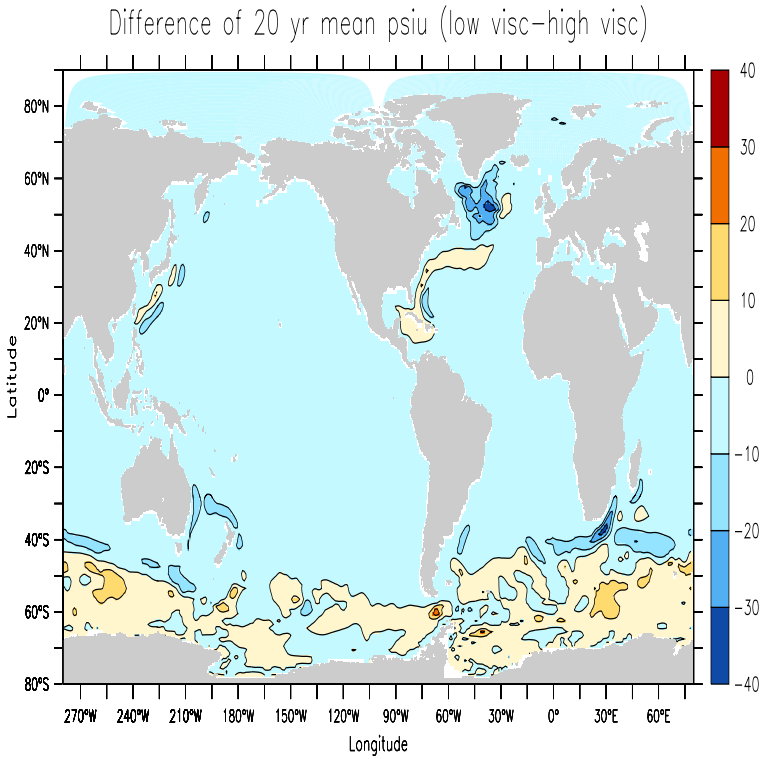

Fig. 16. Difference in the 20 year mean (years 81-100 of the experiment) barotropic quasi-streamfunction $\psi^{(U)}(x,y) = -\int_{y_o}^{y} U(x,y')$ realized in CM2.1 with its horizontal viscosity, and a run with the higher viscosity used in CM2.0. The zero contour line is drawn. Note the larger transport in the Atlantic subpolar region, all boundary currents, and the Antarctic Circumpolar Current.

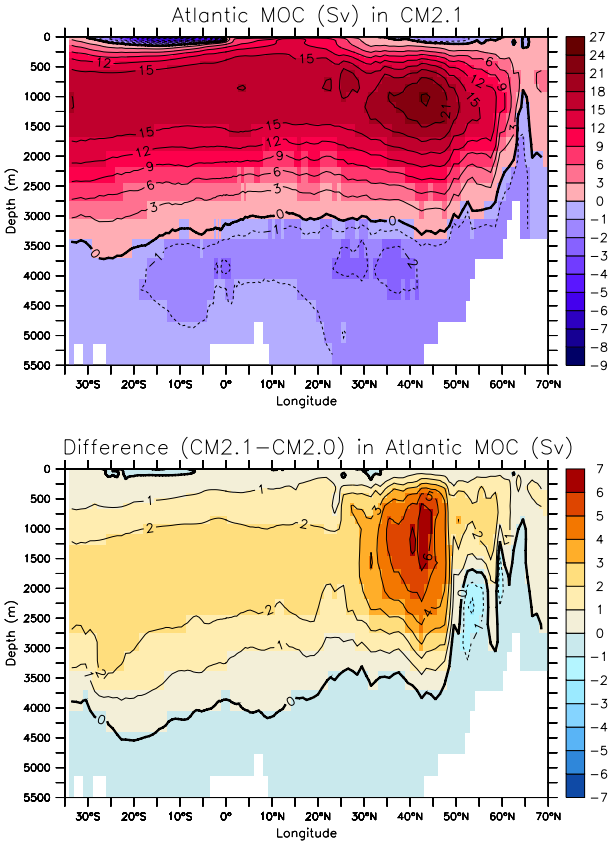

Fig. 17. 20 year mean (years 81–100) for the Atlantic meridional overturning streamfuction in two coupled model experiments. This streamfunction includes both the resolved Eulerian advective transport as well as that due to the Gent et al. (1995) scheme. The top panel is realized using CM2.1. The lower panel is the difference of CM2.1 and another experiment in which the only difference is the use of the larger horizontal viscosity as used in CM2.0. Note the stronger branch in the north, and the larger southward export realized in CM2.1.

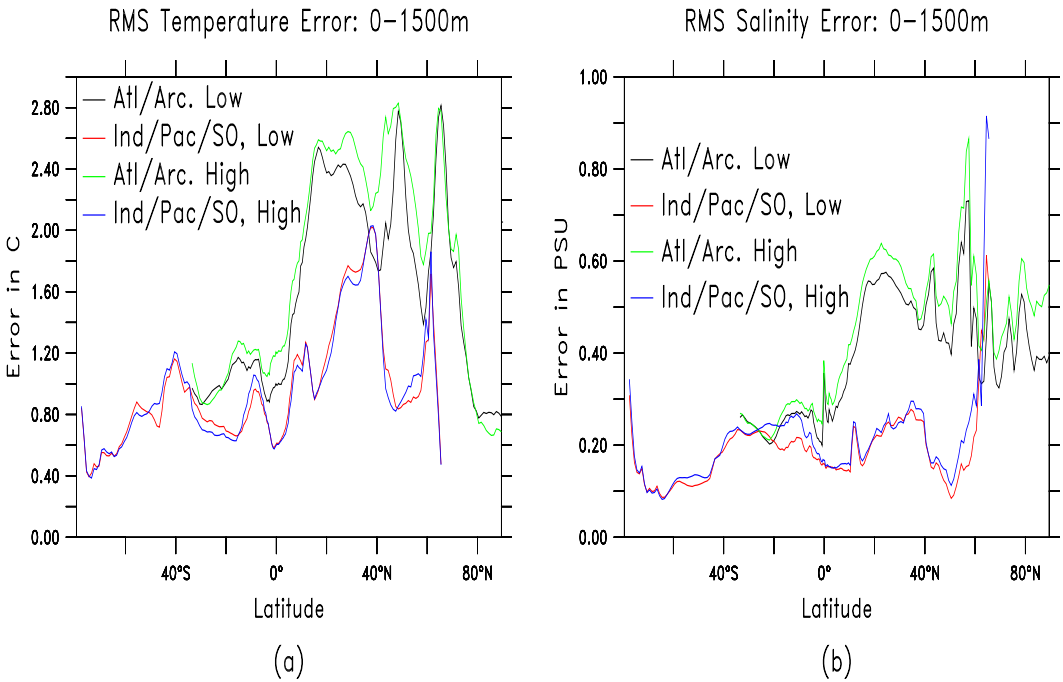

Fig. 18. Zonal mean of the root-mean-square differences over the top 1500m of the low and high extratropical viscosity experiments relative to the atlas of Conkright et al. (2002). Shown here are the errors for potential temperature and salinity over various ocean basins.

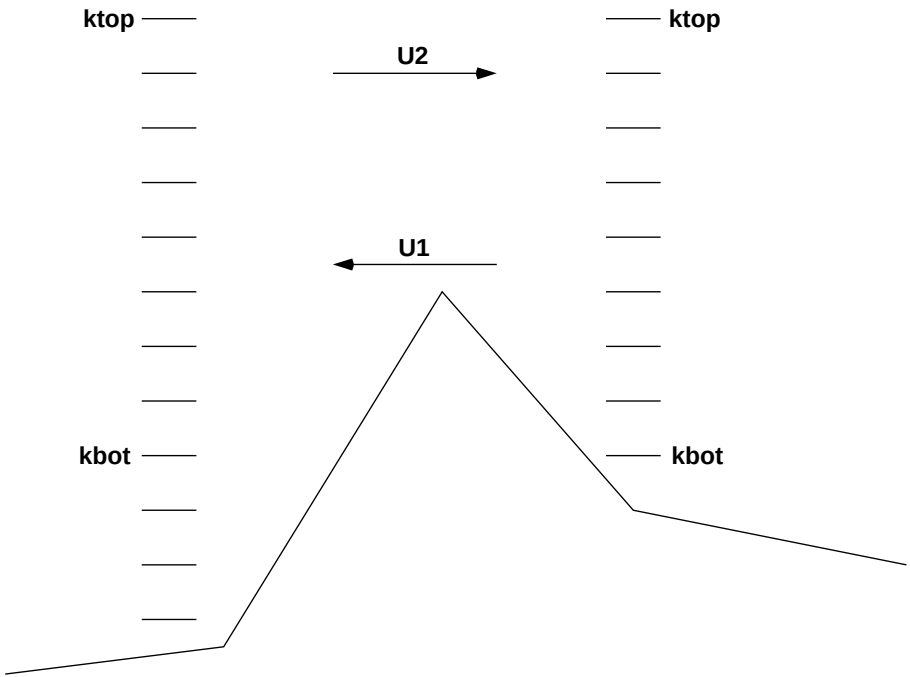

Fig. 19. Schematic of crossland mixing as implemented in MOM4.0. The model's grid mesh is assumed too coarse to explicitly represent the lateral exchange of water masses. For this schematic, we consider a subgrid scale transport U_1 moving in one direction, and U_2 in another. To represent the mixing effects on tracers by these transports, we take the exchange rate U to be the average of the transports $U = (U_1 + U_2)/2$. Crossland mixing occurs between the depth levels $k = k_{\text{top}}$ and $k = k_{\text{bot}}$. If $k_{\text{top}} = 1$, then crossland mixing of volume is allowed in addition to tracer transport. The transport occurs in a way to ensure compatibility between volume and tracer budgets.

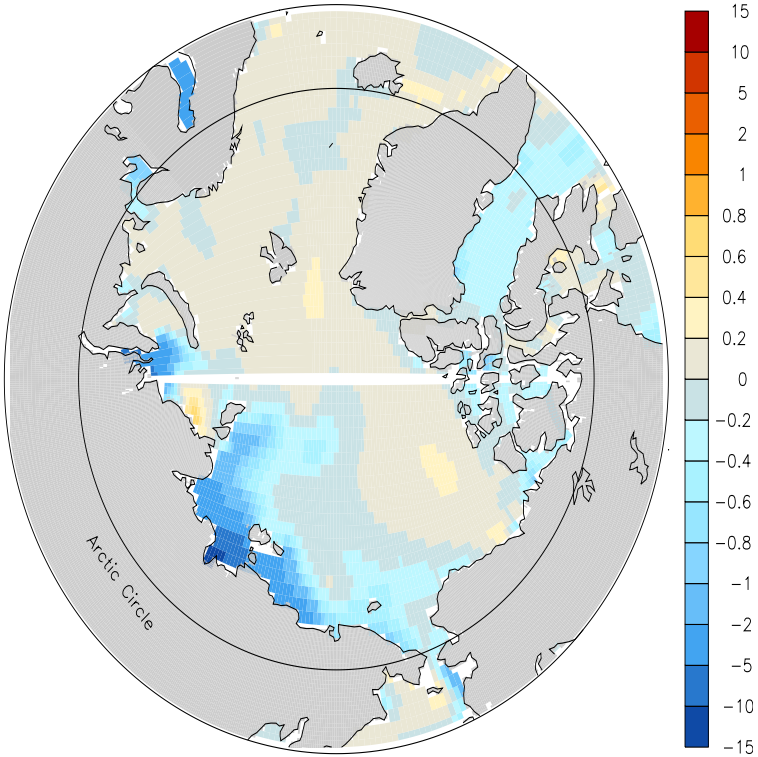

Fig. 20. Difference in surface salinity between the standard CM2.1 experiment, where river runoff is discharged over the upper 40 m of ocean, and test experiment with runoff discharged only over the upper 10 m. The coupled model was run for 20 years, with results from years 16–20 shown here. Earlier pentads show analogous results, with general freshening in the Arctic using 10 m river insertion relative to the standard 40 m insertion.